

Microphysical evolution in mixed-phase mid-latitude marine cold-air outbreaks

Seethala Chellappan,¹ Paquita Zuidema,¹ Simon Kirschler,² Christiane Voigt,² Brian Cairns,³
Ewan C. Crosbie,⁴ Richard Ferrare,⁵ Johnathan Hair,⁵ David Painemal,⁴ Taylor Shingler,⁵
Michael Shook,⁵ Kenneth L. Thornhill,⁵ Florian Tornow,³ and Armin Sorooshian⁶

¹*Department of Atmospheric Sciences, Rosenstiel School, University of Miami, Miami, Florida, USA*

²*Institut für Physik der Atmosphäre, Deutsches Zentrum für Luft- und Raumfahrt (DLR), Oberpfaffenhofen, Germany*

³*Goddard Institute for Space Studies, New York City, New York, USA*

⁴*AMA, Hampton, Virginia, USA*

⁵*NASA Langley Research Center, Hampton, Virginia, USA*

⁶*Department of Chemical and Environmental Engineering, University of Arizona, Tucson, Arizona, USA*

This is a non-peer-reviewed preprint submitted to EarthArXiv under consideration for publication within the AMS Journal of Atmospheric Sciences

17 ABSTRACT: Five cold-air outbreaks are investigated with aircraft offshore of continental north-
18 east American. Flight paths aligned with the cloud-layer flow span cloud-top temperatures of
19 -5 to -12 °C, *in situ* liquid water paths of up to 600 g m⁻², while *in situ* cloud droplet number
20 concentrations exceeding 500 cm⁻³ maintain effective radii below 10 μm. Ice is usually present
21 at cloud initiation. Further downstream, ice particle number concentrations (N_i) of 0.1-2.5 L⁻¹
22 indicate secondary ice production. This is enhanced near cloud top, consistent with collisional
23 breakup of graupel and vapor-grown ice particles, and near cloud base, where ice aggregates near
24 0 °C. Rime-splintering is clearly evident. The highest ice water contents coincide with temper-
25 atures favoring dendritic growth. Warmer clouds and weaker surface fluxes correlate to fewer
26 ice particles. Buoyancy fluxes reach 400-600 W m⁻² near the Gulf Stream's western edge, with
27 updrafts reaching five m s⁻¹ supporting closely-spaced convective cells. Upper-level detrainment
28 maintains a high overall cloud fraction despite decoupled boundary layer vertical structures. The
29 near-surface liquid rainfall rates of three more intense cold-air outbreaks are a maximum near the
30 Gulf Stream's eastern edge, just before the clouds transition to more open-celled structures, and
31 correspond to higher cloud liquid water paths. The milder two cold-air outbreaks transition to
32 lower-albedo cumulus through cloud thinning.

33

34 SIGNIFICANCE STATEMENT: Cold-air outbreaks off of the eastern US seaboard provide
35 dramatic visual examples of cloud transitions from overcast, high-albedo convective clouds to more
36 broken cloud fields. We use data from the recent NASA ACTIVATE (Aerosol Cloud meTeorology
37 Interactions oVer the western ATlantic Experiment) aircraft campaign to examine the microphysics
38 and environmental context of five such outbreaks. We find the clouds are not ice-deprived, but
39 updrafts still supply significant liquid water. Cloud transitions are encouraged through precipitation
40 for the deeper clouds, and, boundary layer warming and drying through entrainment for the thinner
41 clouds. These observations help constrain further modeling studies examining how cloud processes
42 affect the cloud reflectivity, impacting climate prediction, and surface rainfall rates, important for
43 weather forecasting.

44 **1. Introduction**

45 Cold-air outbreaks (CAOs) off of the eastern US seaboard provide dramatic visual examples
46 of cloud morphological transitions, including from closed-cell to more open-celled circulations.
47 Space-based lidar and radar indicate super-cooled liquid clouds overlying melting snow are common
48 over the northwest Atlantic, with a significant latitudinal gradient in snow fraction (Field and
49 Heymsfield 2015; Mülmenstadt et al. 2015; Matus and L'Ecuyer 2017). Model representations of
50 the partitioning between liquid and ice have significant ramifications for the cloud albedo over the
51 southern oceans, with too much ice generating too-dim clouds in CMIP5 models, and too much
52 liquid generating too-bright clouds in CMIP6 models (Zelinka et al. 2020). A warmer climate may
53 encourage more liquid clouds at the expense of ice clouds (the cloud phase feedback) (Mitchell
54 et al. 1989; Frey et al. 2018), in which the smaller size of liquid droplets enhances the reflection
55 of sunlight back to space for the same water mass. If this occurs at temperatures below 0 °C,
56 the liquid clouds can become optically thicker as temperatures warm, because more water vapor
57 is available to convert into liquid (the cloud optical depth feedback) (Tan et al. 2016; Terai et al.
58 2019; Wall et al. 2022; McGraw et al. 2023).

59 In the high-latitude regions, model solar radiation biases are most pronounced behind the cold
60 fronts of synoptic cyclones, where the total cloud cover is dominated by mixed-phase boundary layer
61 clouds (Bodas-Salcedo et al. 2014). CAOs over open water, fed by strong moisture and heat fluxes,
62 can generate significant precipitation, with implications for shipping and coastal communities. The

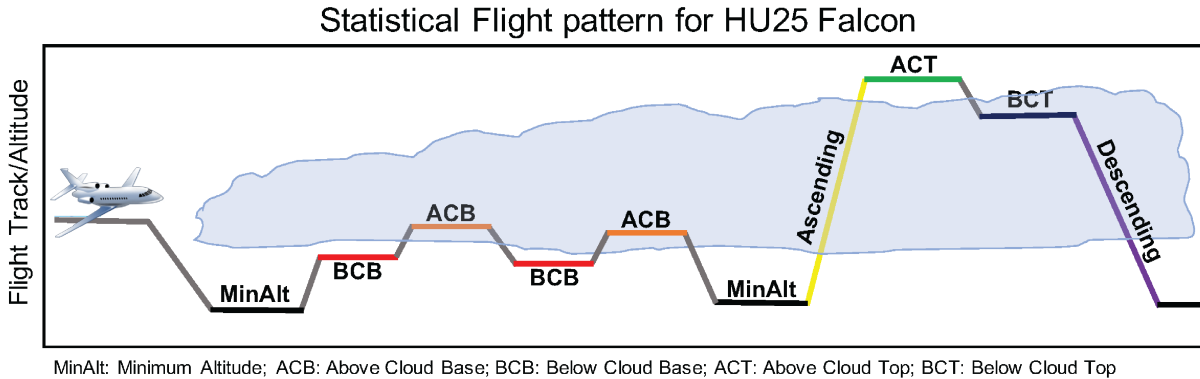
63 precipitation-facilitated evolution from closed- to open-celled cloud organization (e.g., Abel et al.
64 2017) has also remained difficult to model realistically (Field et al. 2017). Interest in improving
65 the understanding, modeling, and prediction of mixed-phase CAOs for both weather and climate
66 has motivated multiple observational campaigns (Wendisch et al. 2019; McFarquhar et al. 2021;
67 Geerts et al. 2022), including over the northwestern Atlantic (Sorooshian et al. 2019).

68 CAOs in the mid-latitudes, because they occur at warmer temperatures than at higher latitudes, can
69 include both rain and ice. Northwestern Atlantic CAOs first flow over the cold near-shore Labrador
70 current and then the warm Gulf Stream (GS). Large air-sea temperature differences support strong
71 surface turbulent fluxes and rapid cloud deepening, with the strong sea surface temperature (SST)
72 gradients encouraging secondary mesoscale circulations (Liu et al. 2014; Naud et al. 2020), and
73 at times of supporting cyclogenesis (Dirks et al. 1988). Of further note is the outflow of urban
74 anthropogenic pollution encouraging high cloud condensation nuclei (CCN) concentrations and
75 cloud droplet number concentrations (N_d) (Corral et al. 2021; Dadashazar et al. 2021; Kirschler
76 et al. 2022; Gryspeerdt et al. 2022). Elevated N_d s can delay precipitation, discouraging cloud break-
77 up and extending cloud lifetime and coverage in subtropical stratocumulus regions (Christensen
78 et al. 2020). For the rapidly-deepening clouds over the Gulf Stream, entrainment of lower free-
79 tropospheric CCN concentrations will dilute the N_d (Tornow et al. 2022). Combined with high
80 cloud liquid water paths (LWPs), precipitation should decouple the surface from the cloud layer,
81 similar to subtropical stratocumulus and subarctic CAOs (Wood et al. 2011; Abel et al. 2017).
82 Modeling studies suggest glaciation can also hasten cloud transitions (Tornow et al. 2021; Atlas
83 et al. 2022) and, given sufficient ice loading, enhance open-celled organization (Eirund et al. 2019).

84 Over the southern oceans, ice enhancement through secondary ice production (SIP) is prevalent
85 in mixed-phase clouds (Yang et al. 2021; Järvinen et al. 2022; Atlas et al. 2022), even in thin
86 clouds with relatively warm cloud top temperatures (Zaremba et al. 2021). This suggests an
87 observational link between ice production and transitions in cloud morphology may also exist
88 for northern mid-latitude CAOs. Overall the modeling of primary and secondary ice production
89 remains highly uncertain (Zhao and Liu 2022). The rime-splintering Hallett-Mossop (HM; Hallett
90 and Mossop 1974) mechanism produces secondary ice when droplets of diameter $< 13 \mu\text{m}$ or > 25
91 μm rime onto large particles, freeze and splinter off as columns (Mossop 1976; Choularton et al.
92 1980). This mechanism is only active between -3 and -8 °C, and is typically the only SIP process

93 represented in models (e.g., Gettelman et al. 2010; Milbrandt and Morrison 2016). At colder
94 temperatures, colliding ice-ice and ice-graupel particles can breakup (Takahashi et al. 1995). This
95 is more common at temperatures favoring dendritic growth ($\sim -15^{\circ}\text{C}$). Larger drops can also shatter
96 upon freezing (Lawson and Zuidema 2009; Lauber et al. 2018) including through riming (Järvinen
97 et al. 2022). Differences in riming fraction encourage a range of fall velocities that support further
98 collisions (Korolev et al. 2020).

99 Here we contribute to this growing literature by presenting analysis from the detailed fetch-
100 following characterizations of five winter days with CAOs over the northwest Atlantic, using recent
101 aircraft measurements from the NASA Aerosol Cloud Meteorology Interactions over the western
102 Atlantic Experiment (ACTIVATE; Sorooshian et al. 2019). The leading question is whether
103 precipitation is needed to encourage transition to cloud structures with lower cloud fractions and
104 albedos, or, if cloud fractions reduce through dry air entrainment from the free troposphere and/or
105 weakened surface fluxes as the boundary layer deepens. ACTIVATE used a unique campaign
106 strategy of flying two stacked planes to acquire a comprehensive set of measurements of both the
107 environmental context and the embedded clouds. The high and low flying planes, both at speeds
108 of $\sim 120 \text{ m s}^{-1}$, aimed to remain within five minutes and six km of each other (Sorooshian et al.
109 2023). The low flying Langley Falcon HU-25 plane followed a set flight pattern (Fig. 1) to collect
110 *in-situ* cloud and aerosol microphysical measurements. At 8-9 km altitude, an accompanying
111 King Air plane hosted the multiwavelength and depolarization sensitive High-Spectral-Resolution
112 Lidar-2 (HSRL2) measuring aerosol and cloud profiles from which cloud top heights are retrieved,
113 and a Research Scanning Polarimeter (RSP) measuring spectrally-resolved shortwave radiances
114 from which cloud optical properties are retrieved. Dropsondes captured thermodynamic and wind
115 profiles (approximately four per flight). Although the plane speed far exceeds the movement of the
116 air mass, the CAOs are quasi steady-state over the course of the day, as inferred from afternoon
117 characterizations that resemble those from the morning flights. This allows us to comment on the
118 CAO evolution, with the five days drawn from March 2020 and January-March of 2021 providing
119 a reasonable range of synoptic and aerosol conditions. The data from the eight research flights
120 occurring on the five days do not support a comprehensive analysis, but do support a framework in
121 which analysis of further data can be inserted, and allow for non-case-specific findings.



122 FIG. 1. Typical Falcon flight sampling plan. The same color coding and nomenclature is applied to each flight
 123 throughout the manuscript. The minimum altitude (MinAlt) legs occurred at ~ 150 m altitude. BCB=below
 124 cloud base, ACB=above cloud base, ACT=above cloud top, and BCT=below cloud top.

125 The paper is organized as follows: Section 2 outlines the datasets used for this study, Section 3
 126 provides the environmental context, and Section 4 details the flights occurring on the five days. This
 127 entails an integrated description of the *in situ* microphysical characteristics with cloud top heights
 128 and temperatures, along with reanalysis-derived surface fluxes and measured vertical velocities.
 129 After describing each flight, we synthesize their information to examine how ice microphysical
 130 quantities and near-surface precipitation depend on cloud-top temperature (T_{ct}), *in situ* temperature
 131 and satellite-retrieved liquid water paths (LWPs). Section 5 integrates the information to develop
 132 a holistic view of mixed-phase cloud evolution in mid-latitude cold-air outbreaks. An online
 133 Supplement provides further supporting documentation.

134 2. Datasets

135 Research flights, detailed in Table 1, lasted near four hours, allowing for both morning and
 136 afternoon flights on select days.

137 a. *In situ* Microphysics

138 A Fast Cloud Droplet Probe (FCDP) and a Two-Dimensional Stereo (2DS) imager, both developed
 139 by the Stratton Park Engineering Company (SPEC) Incorporated and operated by the Deutsches
 140 Zentrum für Luft- und Raumfahrt (DLR), and from a Cloud Droplet Probe (CDP) operated by
 141 NASA Langley, collected the *in situ* cloud water information. The FCDP measures diameters

142 between 3 to 50 μm at a sampling rate of 25 ns, with a nominal size uncertainty of 10% to 50%,
143 and 3%-10% in N_d (Kirschler et al. 2022, and references therein). The aspect ratio of the FCDP
144 particles is gauged so that mainly spherical FCDP particles contribute to the FCDP-derived bulk
145 quantities. Size bin measurements from the FCDP and 2DS probes overlap between 17.1 to 50 μm ,
146 and a combined size distribution spanning 3 to 1465 μm in diameter is constructed, from which
147 the liquid particle number concentrations are identified for three separate radius ranges: cloud ($<$
148 20 μm), drizzle (20-54 μm) and rain ($>$ 54 μm) (Kirschler et al. 2023).

149 The high aerosol loadings advecting off of the populated, industrialized, eastern continental
150 seaboard (Dadashazar et al. 2021; Kirschler et al. 2022) challenge the measurements of the cloud
151 droplet number concentrations (N_{ds}) by both the FCDP and CDP. This is detailed further in the
152 Appendix. We therefore show an average of the FCDP and CDP N_{ds} in the visualizations of each
153 flight. On the 3 February 2021 flight, the FCDP probe iced, and only corrected (see Appendix)
154 CDP data are shown. In the summary analyses we primarily rely on the FCDP cloud probe data.

155 The 2DS data provide IWC, N_i , and ice particle habit information. Ice particles are identified
156 through their asphericity, and spherical ice particles (through e.g. riming) can be missed. The
157 2DS responds to particles of size 5.7 to 1465 μm at a sampling rate of 41 ns, with corrections
158 applied for image distortion, sample area and shattering. The 2DS particle number concentration
159 uncertainty is similar for ice and water (Kirschler et al. 2023). The 2DS detection limit for ice
160 particle concentrations is 10^{-4} cm^{-3} at one Hz sampling, with the analysis limited to non-zero
161 ice particle number concentrations. The optical interaction with small ice columns can generate
162 Poisson focus points in the imagery with the appearance of an 'H' (Vaillant de Guéllis et al. 2019).

163 Individual flight legs last two to four minutes, with most of the analysis relying on leg-means
164 constructed from one-Hz data. Leg-mean N_d are constructed from one-second LWCs exceeding
165 0.01 g m^{-3} and $N_d > 10 \text{ cm}^{-3}$, similar to Kirschler et al. (2023), during Below Cloud Top (BCT),
166 Above Cloud Base (ACB), Below Cloud Base (BCB), and Minimum Altitude (MinAlt, at $\sim 150 \text{ m}$
167 altitude) level legs (Fig. 1). Aircraft ascent rates of $\sim \text{eight m s}^{-1}$, over the four-minute profile legs,
168 imply the plane travels a horizontal distance of $\sim 24 \text{ km}$ during the ascent. This means horizontal
169 cloud heterogeneities can easily become aliased into the profiles.

170 *b. Remotely-Sensed Variables, Reanalysis, and Other*

171 HSRL2 lidar data can also provide an indication of ice and water phase through the ratio of
172 the volume extinction coefficient to the backscattered intensity, known as the lidar ratio (Hu et al.
173 2009). The presence of ice will increase the lidar ratio because of a slight difference in the refractive
174 index between ice and water, above that expected for water spheres of the same size. The lidar
175 ratio is invoked at times.

176 MODIS LWPs are more readily available than those from RSP for the five selected flight days,
177 and can cover a larger spatial domain for each flight. We therefore primarily rely on MODIS
178 LWP to support a comparison across the flights, on the assumption that the retrieval biases are
179 similar across the flights. MODIS values are separated in time by up to two hours from the
180 available profiles. Although the MODIS LWP estimates are likely too low, they do benefit from a
181 compensation between the MODIS cloud optical depth and r_e biases (see fuller assessment within
182 the Appendix).

183 Global High-Resolution satellite Sea Surface Temperature (GHRSSST) contours of 294 K are used
184 to indicate the Gulf Stream (GS). GHRSSST's one km spatial resolution is preferred to the coarser 31
185 km-spatial grid spacing of the ERA5 SSTs, which unrealistically broaden the Gulf Stream (Seethala
186 et al. 2021). Cloud top temperature T_{ctS} are determined from ERA5 temperatures colocated with
187 HSRL-2 cloud-top altitudes. The ERA5 T_{ct} correspond more closely to dropsonde-determined
188 cloud top temperatures than do the MODIS T_{ct} , which can be influenced by surface temperatures
189 (Zuidema et al. 2009). At times, the ERA5 T_{ct} is warmer than the leg-mean temperature of
190 the below-cloud-top (BCT) leg (Fig. S1). Since this is unphysical, the leg-mean *in situ* BCT
191 temperature, when available, is substituted for the ERA5-determined T_{ct} .

192 ERA5 reanalysis also establishes the intensity of a cold-air outbreak using $M = \theta_{SKT} - \theta_{850hPa}$
193 where θ_{SKT} is the 'skin' SST potential temperature, following Papritz et al. (2015) and Seethala
194 et al. (2021). ERA5 buoyancy fluxes (Q_B) are calculated from the latent (Q_L) and sensible (Q_S)
195 fluxes as $Q_B = Q_S * (1 + 0.6q_{2m}) + 0.6Q_L \frac{c_p}{L_v} T_{2m}$, where q_{2m} and T_{2m} are the specific humidity and
196 temperature at 2 meters, c_p is the specific heat of air at constant pressure and L_v is the latent heat
197 of vaporization. Lagrangian forward trajectories are constructed based on ERA5 data at 500 m
198 altitude combined with the HYSPLIT air trajectory model, initialized upstream of the flight path.
199 The flight sampling encompasses approximately one day of the trajectory flow.

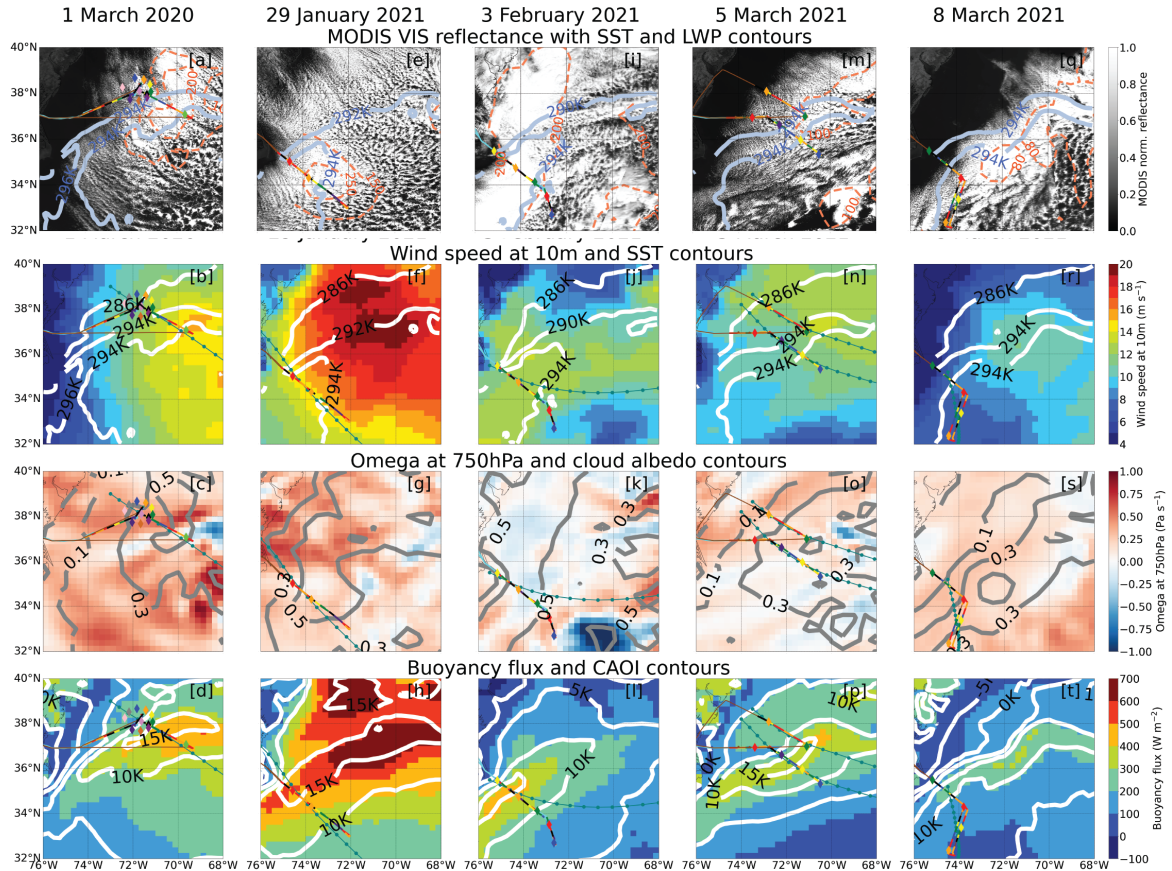
TABLE 1. Dates, research flight numbers, plane participation and dropsonde number for each flight day.

date	morning	am dropsondes	afternoon	pm dropsondes
1 March 2020	RF13, both planes	circle of 11	RF14, both planes. no RSP	2 (downwind)
29 January 2021	RF42, King Air (high flying)	2	RF43, Falcon (<i>in-situ</i>)	0
3 February 2021	RF44, both planes	5	–	–
5 March 2021	RF49, both planes	5	RF50, both planes	2 (downwind)
8 March 2021	–	–	RF51, both planes	4

200 Thermodynamic and wind profiles are provided by the National Center for Atmospheric Re-
 201 search’s NRD41 dropsondes, described further in Vömel et al. (2023). *In situ* vertical velocities
 202 (w), averaged from 20 Hz to a one-second time resolution, are measured with the Turbulent Air
 203 Motion Measurement System (TAMMS; Thornhill et al. 2003). No radar was deployed on either
 204 plane, nor a Nevzorov total water content cloud probe (useful for constraining bin-resolved liquid
 205 water contents), and ice-nucleating particles were not sampled.

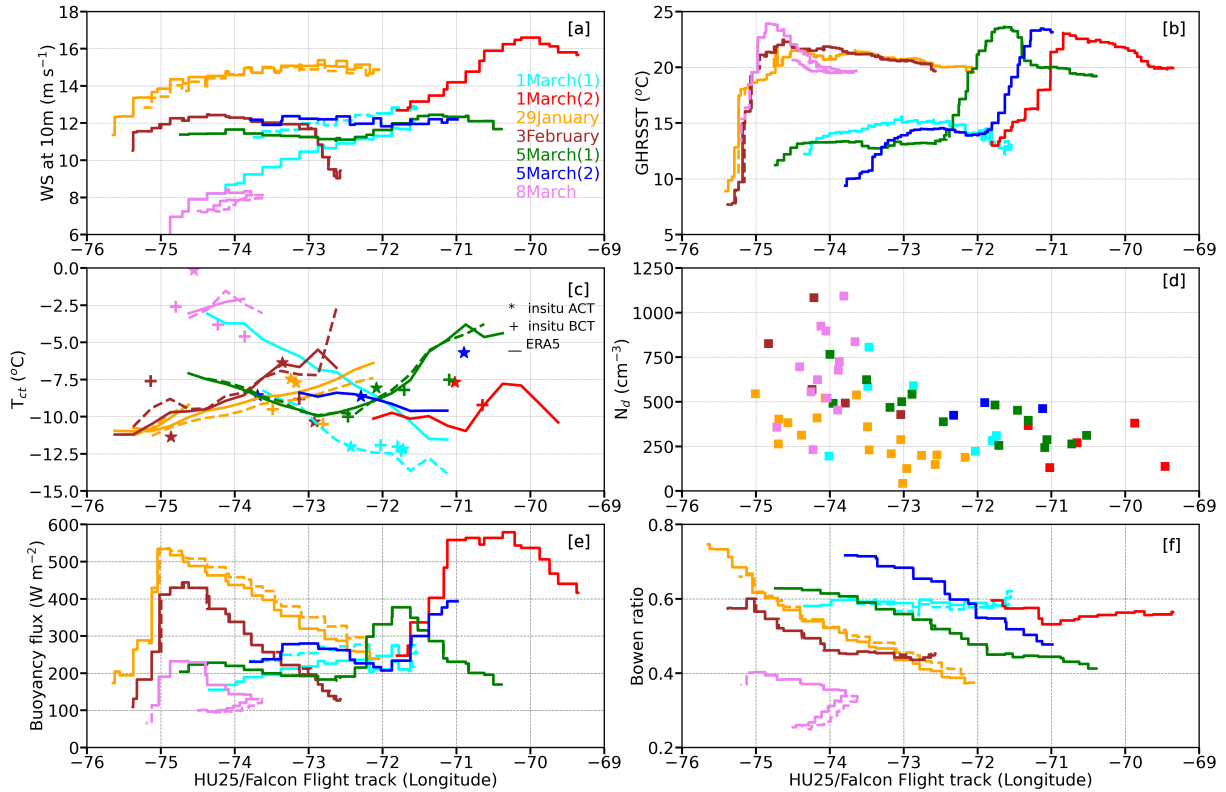
216 3. Overview

217 The five selected flight days are: 1 March, 2020; 29 January, 2021; 3 February, 2021; 5 March,
 218 2021, and 8 March, 2021 (Fig. 2). Three days contained both morning and afternoon flights (March
 219 1, 2020, 29 January 2021 and 5 March, 2021), with Table 1 listing the number of dropsondes per
 220 flight and significant instrument notes. All but the morning flight on 1 March, 2020 followed a
 221 flight track approximately aligned with the Lagrangian boundary layer trajectories (Fig. 2, top row).
 222 All of the flights cross the cold western edge of the Gulf Stream (Fig. 3b). Maximum MODIS
 223 liquid water paths range from 80 g m^{-2} to 250 g m^{-2} . Near-surface ERA5 wind speeds range
 224 from 4 to 20 m s^{-1} , mostly increasing eastward (Fig. 2, 2nd row; Fig. 3a). The increase is in
 225 accord with a surface wind convergence over the warmer waters (Minobe et al. 2008; Small et al.
 226 2008; Plagge et al. 2016). The 750 hPa vertical velocities indicate synoptic subsidence (Fig. 2,
 227 third row). As documented in Painemal et al. (2023), the trough and trough-to-ridge portions of
 228 mid-latitude cyclones give rise to the coastal northerly winds and subsidence that support CAOs.
 229 On 3 February, 2021, the 750 hPa vertical velocities indicate ascent. We show later that 750 hPa
 230 is still within the boundary layer on this day. Surface buoyancy fluxes align well with the Gulf
 231 Stream boundaries (Fig. 2, bottom row) as does the CAO M index.



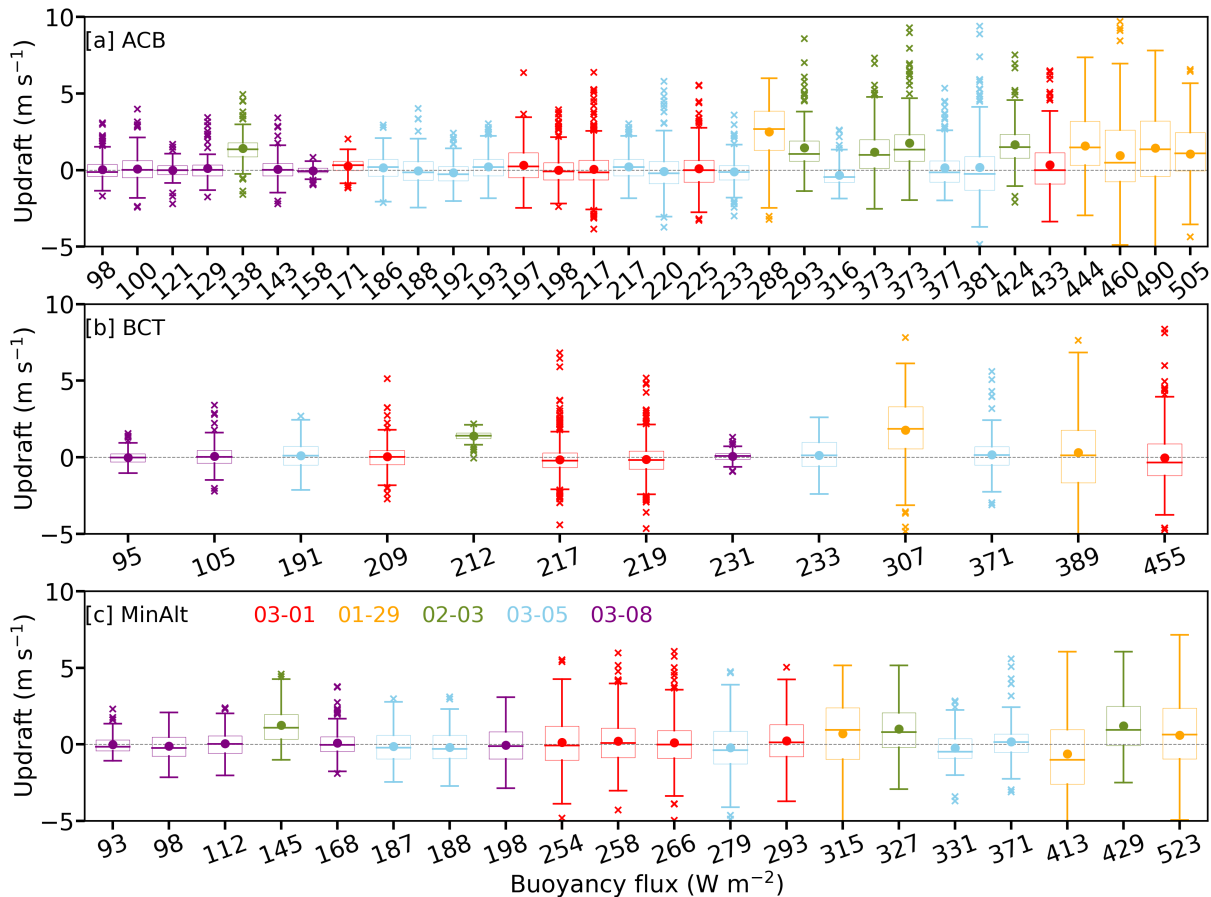
206 FIG. 2. Top row: MODIS visible imagery, with SST contours at 290K, 292K and/or 294K (dusty blue
 207 line), MODIS LWPs at 80,100, 150, 200 and/or 250 g m^{-2} (dashed orange lines), and the Falcon flight tracks,
 208 color-coded by altitude and with dropsonde locations indicated (purple diamonds) for a) 1 March 2020, b) 29
 209 January 2021, c) 3 February 2021, d) 5 March 2021 and e) 8 March 2021. 3 February image is from *Terra*,
 210 the others from *Aqua*. Second row: ERA5 10m wind speed with SST contours overlaid, Third row: ERA5
 211 vertical velocities at 750 hPa (color) with CERES-MODIS cloud albedo in grey contours; and bottom row:
 212 ERA5 buoyancy fluxes (color) overlaid with CAO index (white contours). HYSPLIT trajectories (dark green)
 213 initialized at a)-d): 1 March 2020 15 UTC at 39°N, 73°W, e)-h): 29 January 2021 15 UTC at 36.8°N, 75.5°W,
 214 j)-l): 3 February 2021 14 UTC at 35.5°N, 75.5°W, m)-p): 5 March 2021, 11 UTC at 38.2°N, 74°W (am) and 15
 215 UTC at 38.65°N, 73.5°W (pm), and q)-t): 8 March 2021 trajectory initialized at 15 UTC, 35.2°N, 74.5°W.

239 Along the flight tracks, SST increases can exceed 10 °C at the western edge of the Gulf Stream
 240 (Fig. 3b). The SSTs reach maximum values near 24 °C, decreasing slightly further eastward by a



232 FIG. 3. Meteorology and N_d along the Falcon flight tracks as a function of longitude: a) 10m ERA5 wind speed,
 233 b) SST, c) *in situ* and ERA5 T_{ct} , d) Leg-mean N_d (ACB and BCT), e) ERA5 buoyancy fluxes and f) ERA5 Bowen
 234 ratio, for outbound and inbound (return) flight tracks (solid and dashed lines, respectively). Morning/afternoon
 235 flights on 1 and 5 March indicated by (1) or (2) respectively.

241 few degrees. Cloud top temperatures (T_{ct} s) increase more slowly but consistently with fetch, from
 242 minimum T_{ct} s of ~ -11 °C near the western end, to ~ -5 °C at the eastern end (Fig. 3c). Buoyancy
 243 fluxes and the Bowen ratio are a maximum at the western edge of the Gulf Stream, decreasing
 244 further east as air-sea temperature differences reduce (not shown). *In-situ* leg-mean N_d decrease
 245 with distance offshore from over 1000 cm^{-3} in places to $\sim 200 \text{ cm}^{-3}$. The earliest CAO within the
 246 year, on January 29, 2021, experienced the strongest surface wind speeds, surface fluxes, and M
 247 values of the five days, while the latest CAO, on 8 March, 2021 was the weakest of the five days,
 248 inferred from M and the wind speeds. Corresponding values along the Lagrangian trajectories
 249 correspond well to those perceived during the flights (Fig. S2). This supports the steady-state
 250 assumption that the *in situ* information along the flight track can serve as a proxy for the Lagrangian
 251 evolution, despite the differences in air and aircraft speeds. Dropsonde profiles of temperature, θ



236 FIG. 4. Histograms of 1 Hz vertical velocities as a function of the buoyancy fluxes for a) above-cloud-base,
 237 b) below-cloud-top, and c) minimum altitude level legs. Colors indicate flight date. Means indicated by filled
 238 circles, medians and $\pm 25\%$ percentiles indicated by lines.

252 and relative humidity for each day indicate boundary layer deepening and near-surface warming
 253 as the air masses advect to the east. The relative humidity profiles suggest boundary layers often
 254 remain well-mixed (Fig. S3).

255 Updraft strength increases with the surface buoyancy fluxes, meaning the updrafts are strongest at
 256 the eastern edge of the Gulf Stream (Fig. 4). The upper quartile of the updrafts often exceed two m
 257 s^{-1} (see also Fig. S4), during the MinAlt, ACB, and BCT level legs, with maximum individual 1Hz
 258 values reaching ten $m s^{-1}$. The afternoon flight on January 29, 2021 sampled the strongest updrafts
 259 of the five flight days, followed by 3 February, 2021. One-second downdrafts reach minima of
 260 $-5 m s^{-1}$, with the lowest quartile occasionally stronger than $-2 m s^{-1}$. Updrafts were strongest

261 above-cloud-base (Fig. 4). We will return to Figs. 4 and S4 during the description of the individual
262 days.

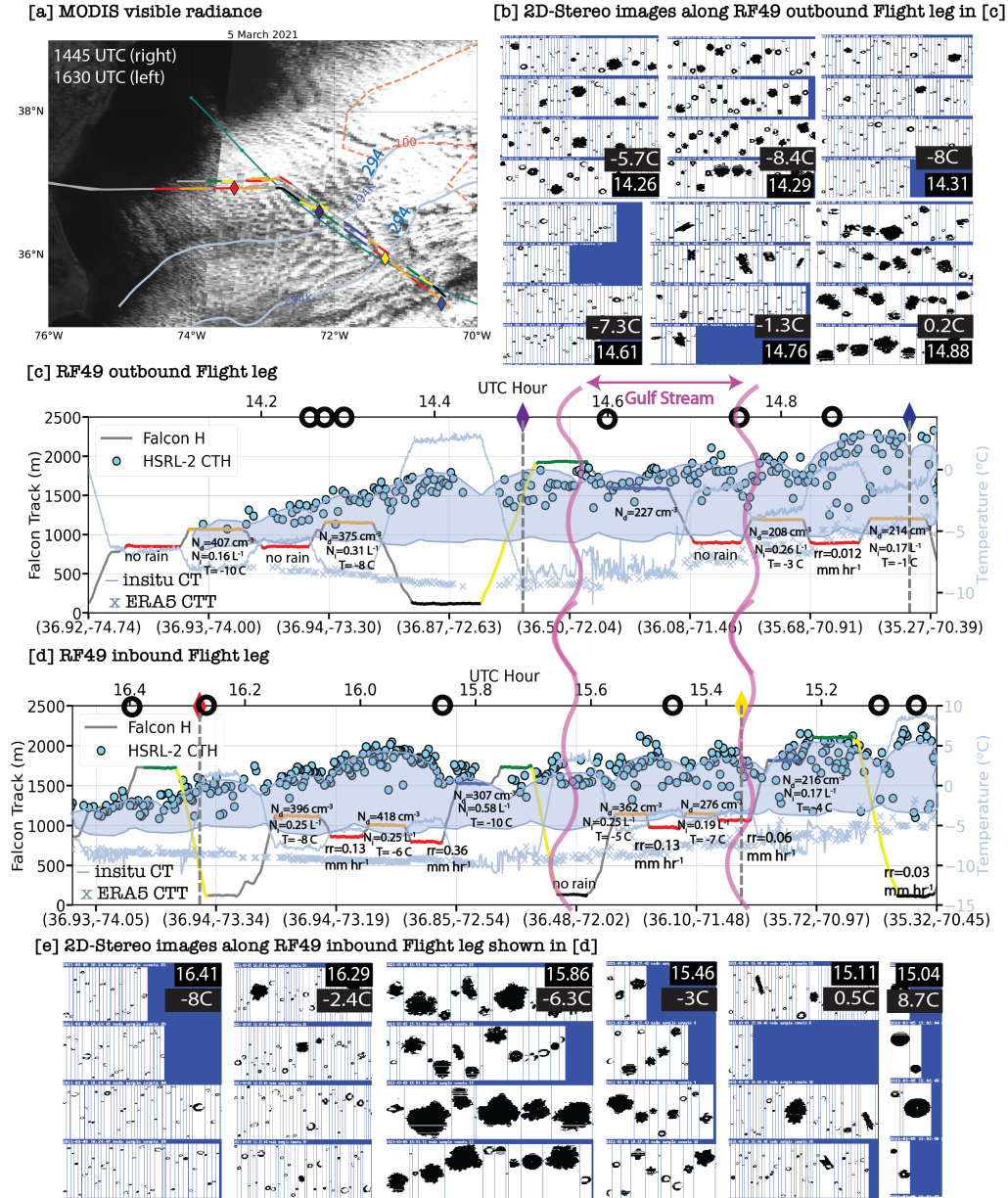
263 **4. Microphysical characterization of the five days**

264 The microphysical characteristics of each day are depicted similarly. Initially, a satellite image
265 is superimposed with the flight track using the color-coding conventions of Fig. 1, followed by
266 height-time series of the flight tracks, their *in situ* temperatures, and the location of selected time-
267 stamped 2DS imagery indicated on the flight tracks. Profiles of microphysical quantities are shown
268 for 1 March 2020, 29 January 2021 and 3 February 2021, with profiles from 5 and 8 March 2021
269 shown in the Supplement.

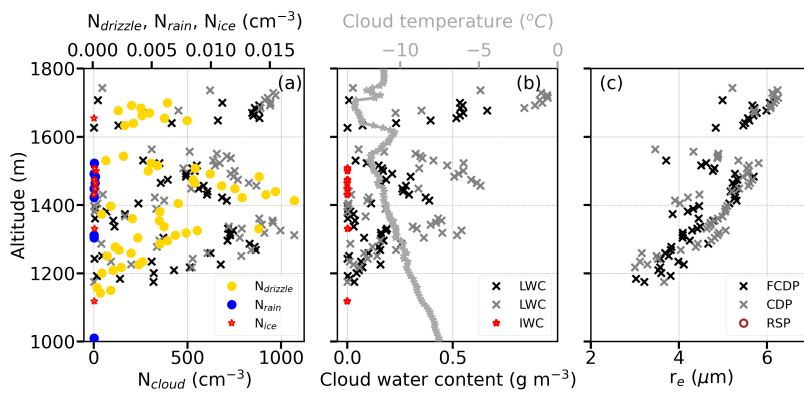
270 *a. 1 March 2020*

271 1) MORNING

272 The morning flight paralleled the western edge of the Gulf Stream, sampling perpendicular to
273 the dominant boundary layer flow. The flight nevertheless first sampled clear air, then thin cloud
274 that continued to deepen, into a region with MODIS-derived LWPs of 100-200 g m⁻², where a
275 circle of 11 dropsondes was released (Fig. 5). Rimed ice was already noticeable within a thin cloud
276 of primarily small super-cooled droplets (Fig. 5c, left-hand image) at an *in situ* temperature of -8
277 °C (Fig. 5b) and leg-mean N_d exceeding 800 cm⁻³. The proximity to upstream clear air suggests
278 primary ice nucleation occurred. A nearby ACB leg during the return leg (16.1 UTC, Fig. 5e)
279 sampled small super-cooled droplets but no ice.

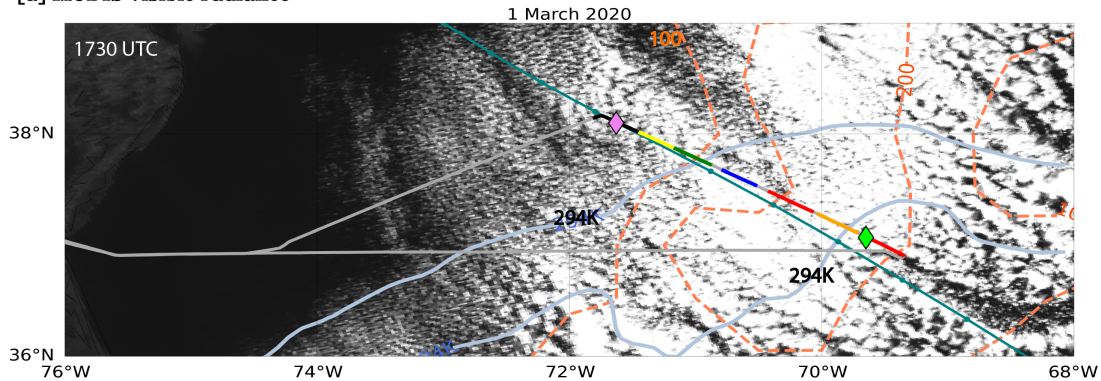


280 FIG. 5. 1 March 2020 morning flight (RF13). a) MODIS visible imagery with flight track superimposed,
 281 color-coded according to Fig. 1 and drosondes (triangles). SST contour of 294K in blue lines, MODIS LWPs
 282 of 100 and 200 g m^{-2} in dashed orange lines. b) HSRL2-inferred cloud top height (circles), altitude flight path
 283 (color-coded), *in situ* temperatures and ERA5 T_{ct} (light blue line and crosses; right-hand y-axis) for the outbound
 284 flight. Circles along upper x-axis correspond to 2DS imagery times in c). d)-e): same as b)-c) for the return
 285 inbound leg; time along upper x-axis increases from right to left. b), d): N_d , N_i indicated for ACB (orange) and
 286 BCT (blue) legs. Cloud depiction is a schematic.

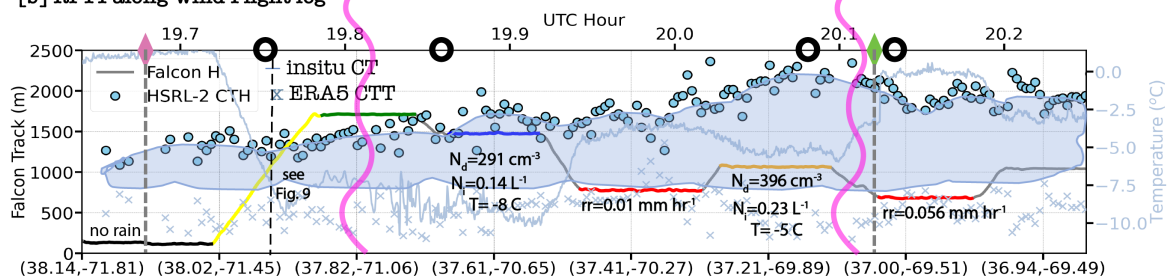


287 FIG. 6. *In-situ* ascent of 1 March 2020 morning (RF13) at 14.4 UTC, 37.65°N, 72.72° E of a) cloud, drizzle,
 288 rain and ice number concentrations (black asterisks, yellow, blue and red filled circles respectively, FCDP+2DS
 289 combined distribution), b) cloud water contents (CDP and FCDP, grey and black asterisks, LWP= 84 and 161
 290 g m^{-2} respectively) and temperature (grey), and c) mean FCDP and CDP droplet effective radius (r_e , black and
 291 grey asterisks respectively).

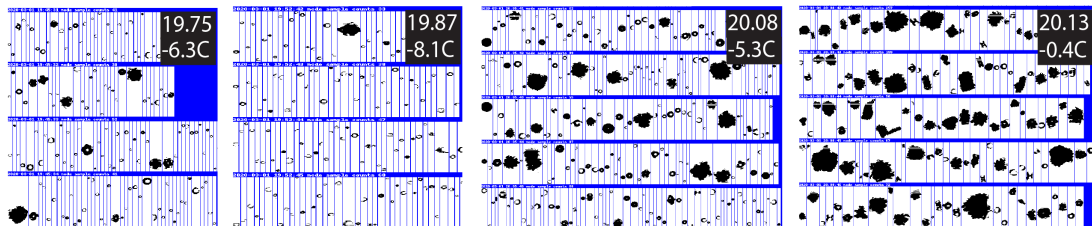
[a] MODIS visible radiance



[b] RF14 along-wind Flight leg



[c] 2D-Stereo images along RF14 along-wind Flight leg shown in [b]



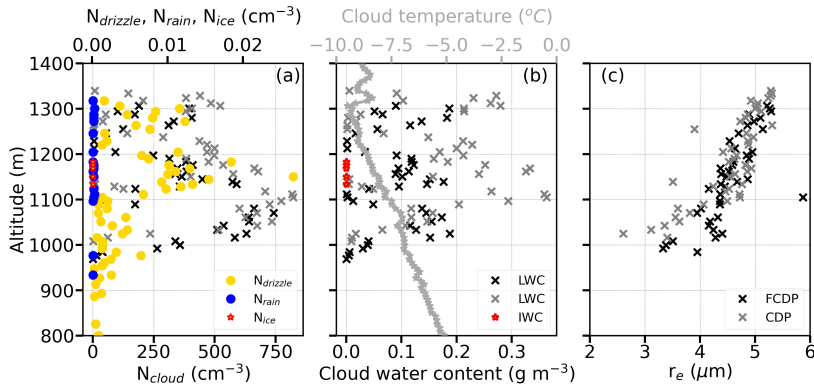
292 FIG. 7. 1 March 2020 afternoon flight (RF14). Similar notation to Fig. 5. No RSP data. 19.75 UTC ascent
 293 profiled in Fig. 8. Two dropsonde locations and times indicated with diamonds. Curved pink lines indicate
 294 location of the Gulf Stream (294K SST contour) throughout.

295 Further within the more developed, stratiform cloud region, snowflakes and large rimed ice
296 particles occur under an ERA5-derived T_{ct} of ~ -12 °C. T_{ct} is near -13 °C for much of the cloud
297 sampling (see *in situ* temperature trace at 14.6 UTC), and dendritic ice growth appropriate to this
298 temperature range is clearly evident throughout the flight. Cloud top heights reach ~ 1.8 km. N_i
299 reaches almost 1 L^{-1} at the northeast end of the flight, too large to still be primary ice production.
300 Only slight precipitation (snow and a few rimed ice particles) is detected on the easternmost MinAlt
301 leg at 14.8 UTC, at temperatures barely above 0 °C. The leg-mean N_d decreased within the more
302 developed cloud near the dropsonde circle, consistent with dilution through cloud top entrainment
303 (Tornow et al. 2021). Dropsondes show mostly well-mixed boundary layers (Fig. S3). The flight
304 did not reach beyond the overcast stratiform cloud region, nor entered above the demarcated Gulf
305 Stream.

306 The first profile, an ascent through cloud with a LWP of $\sim 100 \text{ g m}^{-2}$ (Fig. 6), shows an inversion-
307 capped cloud layer reaching ~ 1.5 km, with a separate thin cloud layer between 1.6 to 1.8 km.
308 Surface buoyancy fluxes reach 200 W m^{-2} (Fig. 3e), supporting vertical velocities of $2\text{-}4 \text{ m s}^{-1}$
309 (Figs. 4 and S4). Although such updrafts may be strong enough to puncture an existing cloudtop
310 inversion and form a new cloud layer aloft, none of the dropsondes show such a marked temperature
311 structure (Fig. S3). Instead, the dropsondes captured a range of inversion heights, often capped
312 by multiple stable layers. This is more consistent with a range of cloud top heights and likely
313 the plane exited one convective cell and entered the top of another. No ice was detected in the
314 uppermost, coldest cloud layer. Cloud-top r_e remain below six μm , consistent with N_d exceeding
315 700 cm^{-3} . Some ice was sampled within the profile near the top of the middle layer, at temperatures
316 between -10 to -12 °C, with vapor-driven particle growth evident nearby in 2DS imagery in the
317 same temperature range (e.g., snowflakes at Fig. 5c at 14.53 UTC and the next hour). N_i and IWCs
318 are highest at cloud temperatures between -9.5 °C and -12.5 °C, outside the HM temperature range
319 for SIP, but colocated with some drizzle and the liquid water content (LWC) maximum (Fig. 6),
320 suggesting another rime-related SIP may be active.

321 2) AFTERNOON

322 Conditions during the afternoon flight were visually similar to the morning flight, but now
323 the research flight was well-aligned with the boundary layer flow, crossing over the 294 K SST



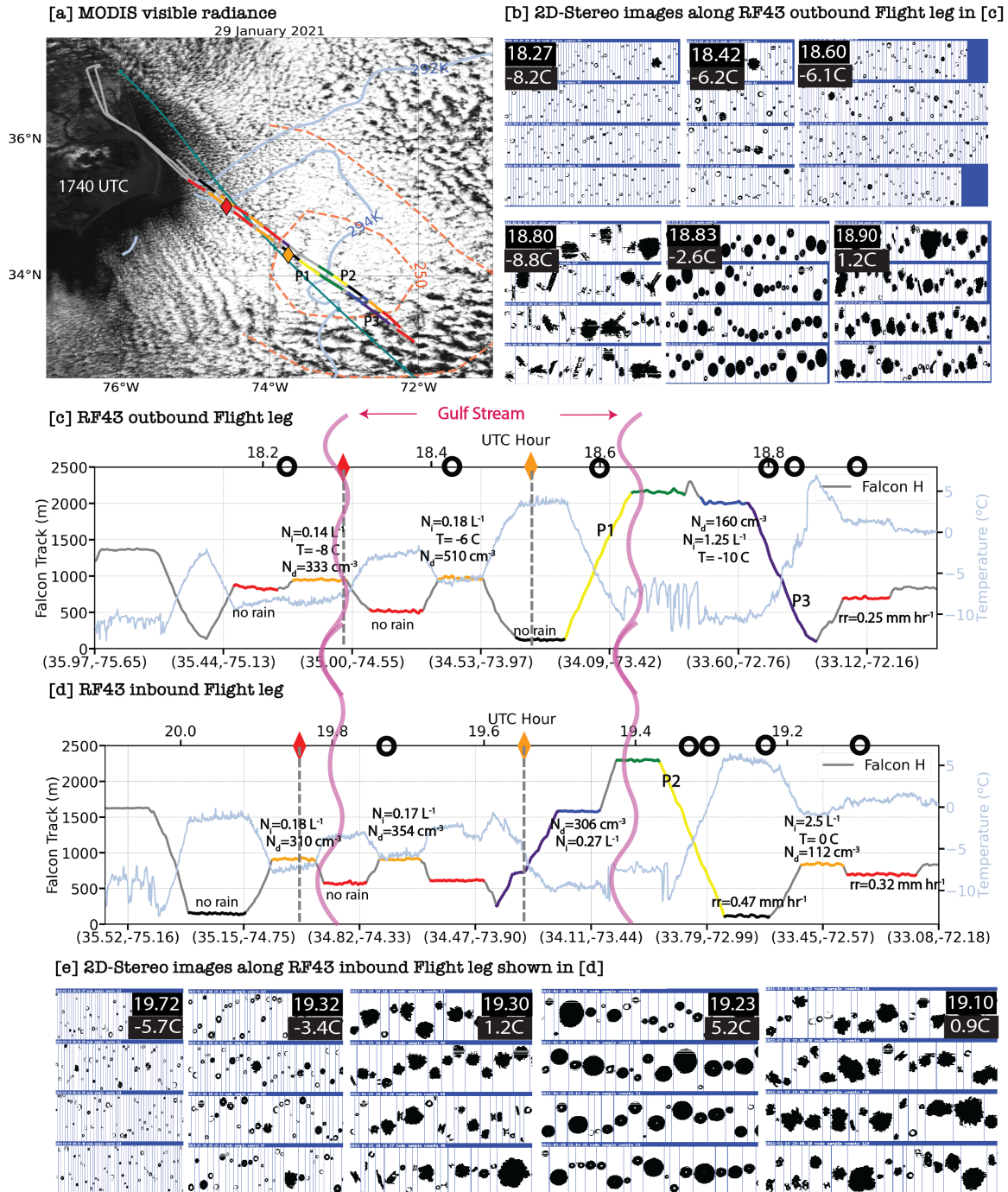
343 FIG. 8. 1 March 2020 afternoon (RF14) *in-situ* ascent at 37.95°N, 71.31°E, 19.75 UTC of a) cloud, drizzle,
 344 rain and ice number concentrations, FCDP+2DS, (b) cloud water content and temperature (CDP and FCDP, grey
 345 and black asterisks, LWP= 30 and 51 g m⁻² respectively), and (c) droplet effective radius (r_e).

324 contour outlining the Gulf Stream at 19.8 UTC and briefly experiencing the cloud transition into
 325 more open-celled convection past the eastern edge of the Gulf Stream at 20.2 UTC (Fig. 7). Just
 326 before the Gulf Stream, an ascending profile sampled rimed ice within a layer of predominantly
 327 super-cooled water droplets at temperatures ~ -6 °C (Fig. 7c, first image). N_d decreases with
 328 altitude and is slightly less than in the morning (Fig. 8; 250-400 cm⁻³ versus 500-800 cm⁻³). The
 329 temperature inversion is capped by at least one additional stable layer similar to the dropsonde
 330 profiles, consistent with the idea that the boundary layer deepening may be occurring in discrete
 331 intervals as opposed to a smooth increase in height.

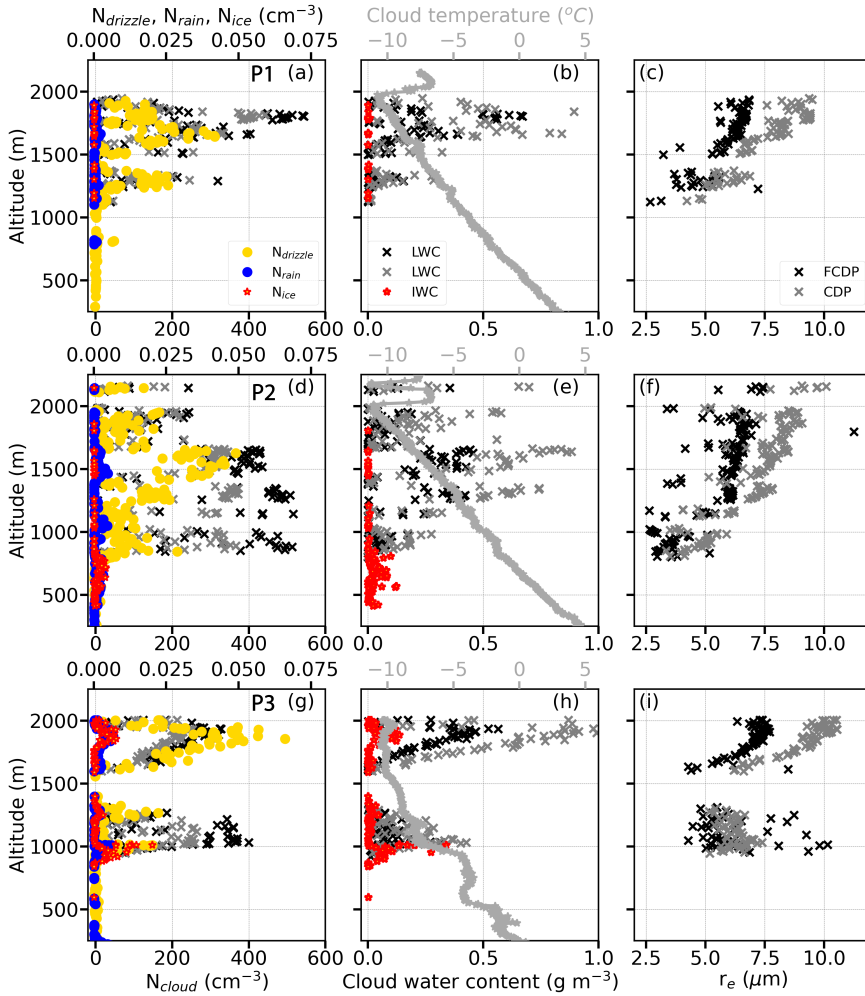
332 Just east of the Gulf Stream, MODIS LWPs reach 200 g m⁻², with cloud top heights reaching 2.3
 333 km (Fig. S3, lime-green dropsonde) above a slightly stable boundary layer ($\frac{\partial\theta}{\partial z} \sim 2$ K km⁻¹). The
 334 cloud base warms as the flight progresses, with the first below-cloud-base leg (BCB, red) occurring
 335 at ~ -3 °C and the second near 0 °C, despite similar altitudes of ~ 700 m. Light rain is mixed with
 336 some aggregates during the first BCB leg (not shown). Rain increases to 0.056 mm hr⁻¹ in the
 337 second BCB leg amidst large snow aggregates falling towards even warmer temperatures (Fig. 7c,
 338 last image). Thus rain is measured just prior to the transition region to a more open-celled cloud
 339 structure. Rimed ice particles co-exist with supercooled droplets in the HM temperature range
 340 (2DS image at 20.08 UTC in Fig. 7c and Fig. 8), with some (poorly-resolved) columns apparent at
 341 20.13 UTC. N_i increases towards the east as the clouds deepen, as does the rainrate below cloud
 342 base (Fig. 7b).

346 *b. 29 January 2021*

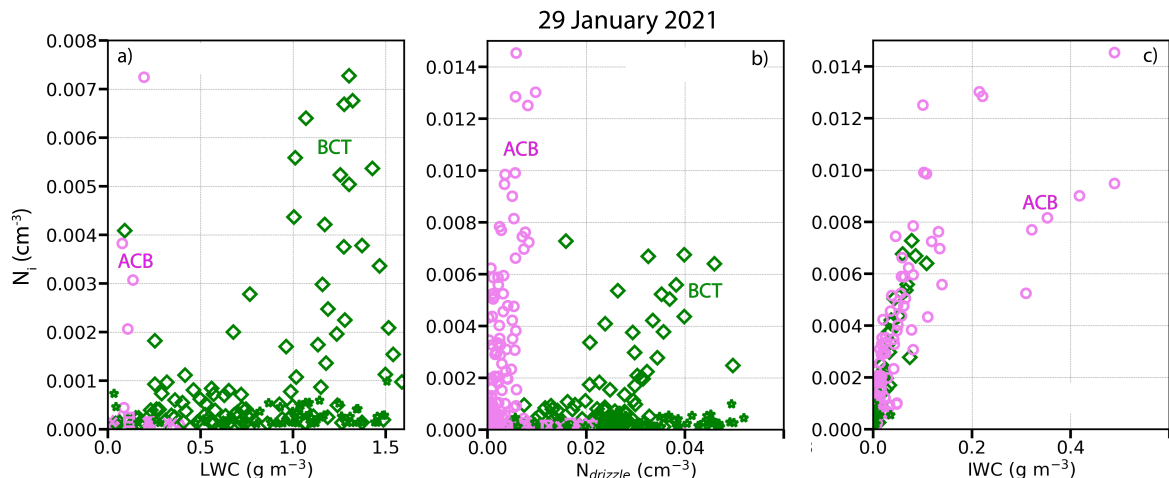
347 This CAO is the earliest within the seasonal cycle, with the 294 K SST contour barely reaching
348 the ACTIVATE domain from the south (Fig. 2e). The morning and afternoon flights follow similar
349 boundary layer flows, sampling mostly visually-overcast regions with MODIS LWPs $> 250 \text{ g m}^{-2}$
350 and just able to reach the open-celled cloud structure east of the Gulf Stream. ERA5 10-m winds
351 exceed 14 m s^{-1} in places (Fig. 3a), supporting buoyancy fluxes $> 500 \text{ W m}^{-2}$ at the western
352 GS edge (Fig. 2h), and 1 Hz w_s exceeding 5 m s^{-1} (Figs. 4, S4). The morning-only high-flying
353 King Air plane released two dropsondes, near the eastern and western edges of the Gulf Stream
354 respectively, separated by a distance of $\sim 100 \text{ km}$. These indicate a deepening of a relatively
355 well-mixed boundary layer from $\sim 1.7 \text{ km}$ to $\sim 2 \text{ km}$ (Fig. S3), with the near-surface relative
356 humidity decreasing to 50% - dry enough to desiccate sea salt (Ferrare et al. 2023).



357 FIG. 9. 29 January 2021 afternoon (RF43). Similar notation to Fig. 5. Morning dropsonde locations shown.
358 See Fig. 10 for *in situ* profiles P1, P2 and P3.



359 FIG. 10. 29 January 2021 afternoon (RF43) *in-situ* profiles organized from west (top) to east (bottom).
 360 a)-c): P1, ascent at 18.6 UTC, 34.13°N, 73.46°W (FCDP+2DS, CDP+2DS LWP=93, 225 g m⁻² resp.) over the
 361 eastern flank of the Gulf Stream. d)-f): P2, 19.35 UTC ascent at 33.83°N, 73.04°W (FCDP+2DS, CDP+2DS
 362 LWP=121,260 g m⁻² resp.), just east of the eastern GS 294 K SST contour. g)-i): P3, descent at 18.8 UTC,
 363 33.43°N, 72.55°W (FCDP+2DS, CDP+2DS LWP=154, 305 g m⁻² resp.), further east of the Gulf Stream.
 364 Conventions as in Fig. 6.



365 FIG. 11. N_i vs a) LWC, b) $N_{drizzle}$, and c) IWC for the ACB (pink) and BCB (green) legs from 29 January
 366 2021 (RF43), using 1Hz data. Note y-axis range for N_i differs between a) and b),c).

367 The locations of the morning dropsondes are superimposed on the *in situ* information collected
 368 during the afternoon RF43 flight in Fig. 9. Prior to crossing over the western GS edge at ~ 18.3
 369 UTC, the first within-cloud ACB leg measured a leg-mean N_d of 330 cm^{-3} at a temperature of -8.2
 370 $^{\circ}\text{C}$. A rimed/aggregated ice particle is already present within the cloud of small droplets (see first
 371 image in Fig. 9b). The proximity to clear-sky upwind again points to primary ice production, as
 372 opposed to secondary. Deeper clouds further east reach an *in-situ* T_{ct} near $-10 \text{ }^{\circ}\text{C}$ at 18.75 UTC.
 373 Rimed and aggregated snow particles are detected, along with a few columns (see e.g. 2DS image
 374 at 18.8 UTC). The thickest cloud is situated at and east of the eastern GS edge. By then, the BCB
 375 leg temperature has risen to $2 \text{ }^{\circ}\text{C}$, and leg-mean rain rates reach 0.25 mm hr^{-1} , increasing to 0.47
 376 mm hr^{-1} for the lower MinAlt leg (note these rainrates are based on 1Hz samples exceeding 0.01
 377 mm hr^{-1} only). Snow aggregates below cloud base become rain by 150 m above the ocean surface,
 378 preceding the transition to a more open-celled cloud morphology.

379 Three *in situ* profiles occur within 45 minutes and 110 km of each other, either directly over
 380 or slightly east of the Gulf Stream (Fig. 10). These are shown arranged from east to west (top
 381 to bottom) in Fig. 10, with profile P3 preceding profile P2 in time. For all three profiles, the
 382 T_{ct} and cloud top height remain at -10 to $-11 \text{ }^{\circ}\text{C}$ and 2 km respectively. Precipitation in both
 383 the ice and liquid phase increase with fetch. *In situ* profile LWPs increase from 230 to 440 g
 384 m^{-2} , yet *in situ* cloud-top effective radii remain at $9 \text{ } \mu\text{m}$ or below, because of the high number

385 of droplets (maximum N_d ranges between 400-500 cm^{-3}). The profiles appear to sample two (or
386 more) distinct cloud layers, although this may reflect slant-path ascent wherein up- and downdrafts
387 produce different cloud bases.

388 Profile P1, an ascent at 18.6 UTC over the eastern GS, samples a well-mixed boundary layer in
389 stratiform conditions (Fig. 10a-c). The 0°C level is at ~ 500 m, below the lower cloud base at 1.2
390 km, and the cloud top is strongly capped by a 5K temperature inversion (Fig. 10b). N_d increases
391 to 550 cm^{-3} near the upper cloud top, within the highest LWCs of the profile. The increase in
392 N_d with height suggests the N_d is reduced lower down primarily through collision-coalescence.
393 Despite cloud-top r_e of only $\sim 8 \mu\text{m}$, some drizzle is present higher up, capable of initiating
394 collision-coalescence, and some ice particles are detected at temperatures between -4 to -10°C .

395 The ascent profile P2 approximately 50 km further east occurred at 19.35 UTC during the return
396 flight. A lower cloud base at approximately 800 m compared to P1 suggests the plane went through
397 an updraft bringing up moist air (Fig. 10d-f). An additional thin cloud layer exists at 2.2 km altitude
398 above the existing inversion, similar to Fig. 6. Buoyancy fluxes exceeding 500 W m^{-2} (Fig. 2h)
399 coincide with updrafts in the preceding ACB leg that reached 5 m s^{-1} in places, for a leg-mean w
400 of 3.5 m s^{-1} . These may have punctured through the capping cloud inversion to produce the thin
401 cloud layer aloft. N_d decreases from 600-650 cm^{-3} at cloud base to $\sim 300 \text{ cm}^{-3}$ near cloud top,
402 also consistent with dilution through entrainment (Tornow et al. 2022).

403 Graupel coexists with super-cooled water at the upper levels. The 0°C level has risen 100-150 m
404 from the location of P1, to 600-650 m, with a stable layer below the cloud base indicating melting-
405 induced cooling. Larger snow aggregates are apparent at temperatures slightly above melting,
406 transitioning to rain by the 5°C of the MinAlt leg (Fig. 9e, middle three images). The MinAlt
407 leg-mean rainrate is relatively high at almost 0.5 mm hr^{-1} . Both the IWC and N_i increase near or
408 just below the cloud base within the P2 profile. Prior to P2, on an ACB leg, the highest N_i of the
409 five flight days, 2.5 L^{-1} , was measured at near melting temperatures (Fig. 9d, 19.15 UTC). 2DS
410 imagery at 19.1 UTC indicates many ice (graupel) particles and snow aggregates of different sizes.
411 We speculate surface melting on ice particles is enhancing ice aggregation, thereafter breaking up
412 into more N_i through collisions (Fabry and Zawadzki 1995).

413 Further east by 50 km, the descent profile P3 at 18.8 UTC on the outgoing flight took place
414 just west of an open-celled cloud structure (Fig. 10g-i). The descent followed a BCT leg with

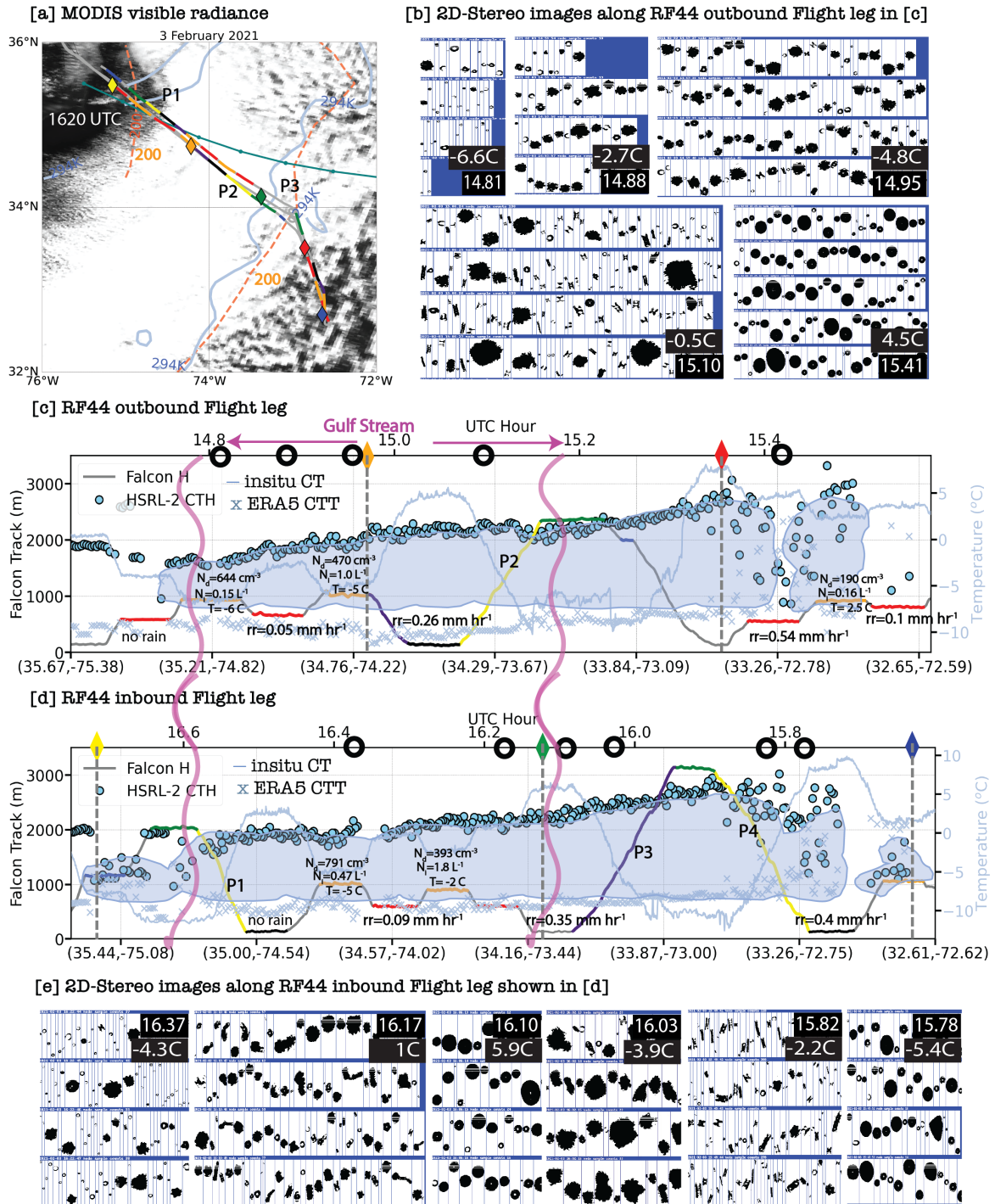
415 a leg-mean N_i of 1.25 L^{-1} (1 Hz $N_i > 0$ samples only) at a temperature of -10.5°C . During the
416 descent, 2DS imagery first indicates large graupel and aggregates (18.8 UTC in Fig. 9b) followed
417 by rain drops by 18.83 UTC. The subsequent BCB leg samples mostly aggregates and graupel
418 at 18.9 UTC (Fig. 9b) but with a leg-mean rainrate of 0.25 mm hr^{-1} , at 1°C . The *in situ* P3
419 temperature profile is erratic (Fig. 10h), suggesting icing may have at times influenced the aircraft
420 temperature sensor.

421 Fig. 10g-h show a clear correlation between N_i and $N_{drizzle}$ at the upper levels, as well as
422 between IWC and LWC, suggesting rime-splintering is still occurring at temperatures too cold for
423 HM ice production. Droplet shattering would be inefficient given the mean effective radius of
424 $\sim 8 \mu\text{m}$. Riming, besides increasing the IWC, also increases variations in the particle fall speeds
425 and encourages breakup through graupel-graupel collisions (e.g., 2DS imagery of a spheroid and
426 elongated ice particle together at 18.8 UTC in Fig. 9b). Increased N_i and IWC are also present at
427 cloud base, similar to P2, consistent with enhanced aggregation enabled by a liquid layer on the
428 surface of ice.

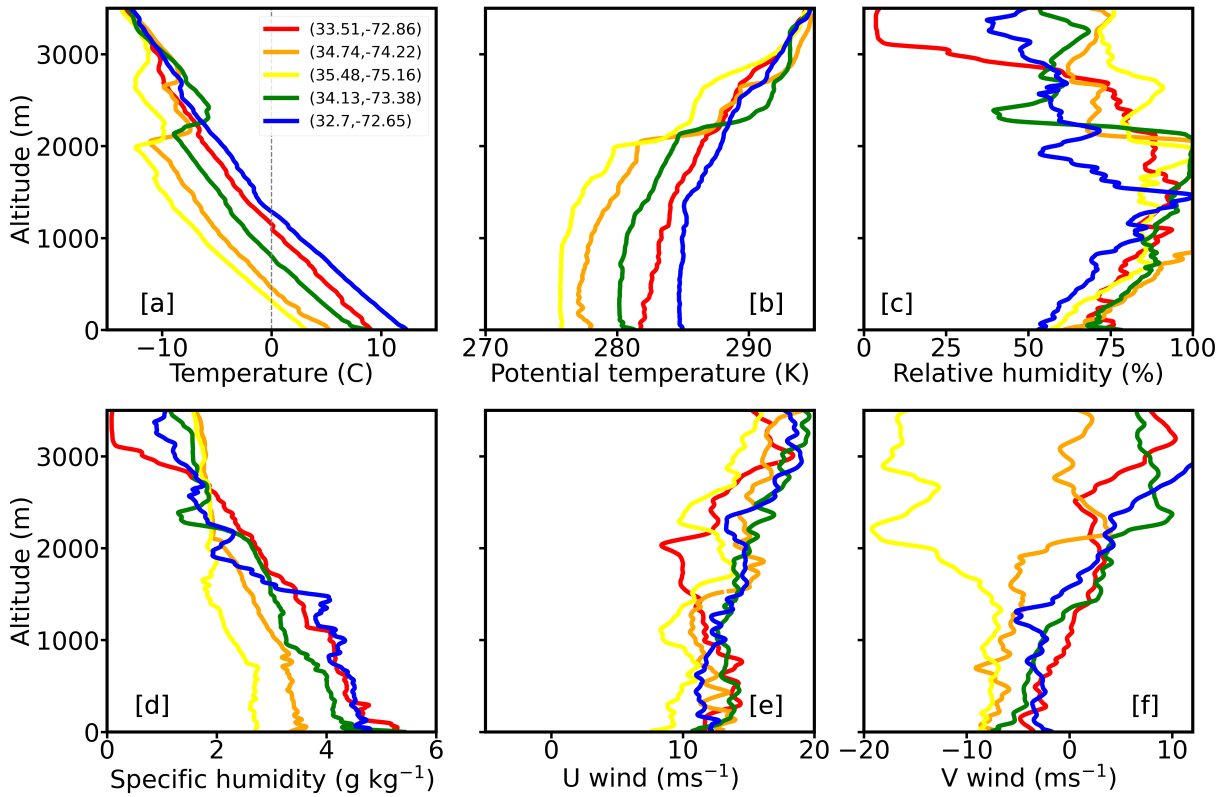
429 Overall the *in situ* data indicate N_i increases with fetch to the east, shifting to the liquid phase
430 near the surface, before thick clouds transition into more open-celled structures. The highest N_i
431 documented within the five days occurred on this day. N_i is clearly enhanced at both upper and
432 lower clouds levels (see Fig. 10g in particular), summarized in Fig. 11, and more than one SIP
433 mechanism appears to be at play. At upper levels, N_i increases with increasing LWC, $N_{drizzle}$ and
434 IWC at temperatures $\sim -10^\circ\text{C}$ (Fig. 11), consistent with riming followed by collisional breakup,
435 and maybe droplet freezing, although the small drop sizes discourage the latter. Near or slightly
436 below cloud base, at temperatures near 0°C , the most pronounced increase in N_i occurs with IWC
437 (Fig. 11c), a relationship that seems best explained by a surface layer of quasi-liquid enhancing
438 aggregation and thereby N_i through collisional breakup. Precipitation doesn't set in until the eastern
439 GS edge, perhaps delayed by the high N_d . By then, the air near the surface is warm enough that
440 snow aggregates melt into rain before reaching the surface (e.g., 19.10 UTC BCB leg and 19.23
441 UTC MinAlt leg 2DS imagery in Fig. 9e).

442 *c. 3 February 2021*

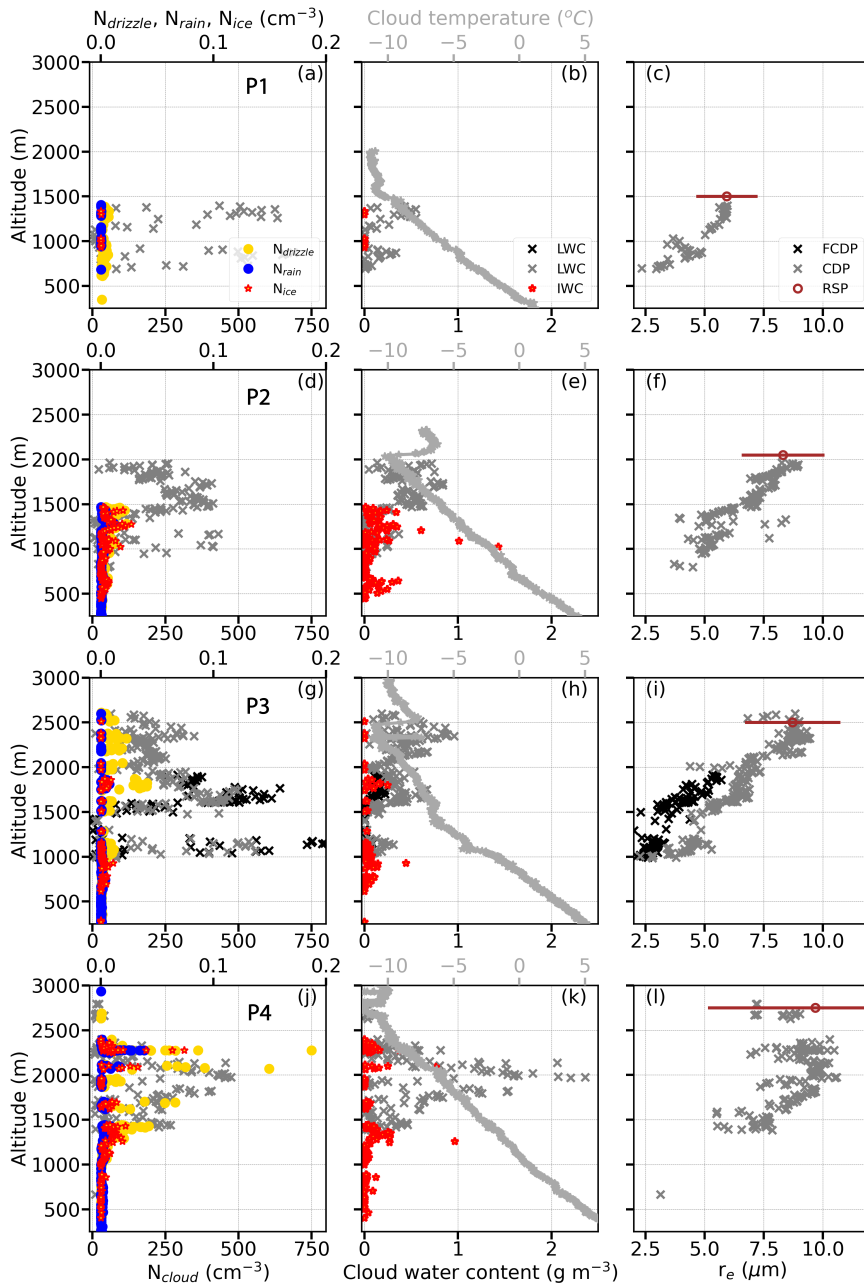
443 Both planes participated in this morning-only flight, flying through/over thick stratiform cloud
444 above the Gulf Stream for which MODIS-derived LWPs exceed 200 g m^{-2} in places (Fig. 12),
445 reaching the cloud transition region. The FCDP failed from 15.1 UTC to 16.1 UTC, increasing
446 reliance on the CDP data. The stratiform cloud is visually the brightest of the five flight days
447 (Fig. 2), with leg-mean N_d s exceeding 700 cm^{-3} at the western GS edge. The Gulf Stream was
448 broader than on Jan. 29, and surface winds of 12 m s^{-1} were weaker than those on January 29, 2021,
449 by $2\text{-}3 \text{ m s}^{-1}$ (Fig. 2). Buoyancy fluxes exceeded 400 W m^{-2} at the western GS edge, corresponding
450 to a 14 K air-sea temperature difference. These continue to support vertical velocities exceeding 5
451 m s^{-1} (Figs. 4 and S4).



452 FIG. 12. 3 February 2021 morning (RF44). Similar notation to Fig. 5. FCDP cloud probe iced from 15.1 UTC
 453 until midway through P3 descent at 16.1 UTC (profiles shown in Fig. 14).



454 FIG. 13. 3 February 2021 morning (RF44) dropsonde profiles of a) temperature, b) potential temperature, c)
 455 relative humidity, d) specific humidity, e) zonal wind, and f) meridional winds. Colors follow the diamonds in
 456 Fig. 12: yellow dropsonde is west of the GS, orange over the middle of the GS, green at GS eastern edge, red
 457 and blue just before and within the open-celled cloud structure, respectively.



458 FIG. 14. Four *in situ* profiles from 3 February 2021 morning flight (RF44), organized from west (top) to east
 459 (bottom). FCDP (black asterisks in g-i)) was iced but for a portion of the P3 descent. a)-c): P1 ascent at 16.55
 460 UTC at 35.11°N, 74.67°W on the return (inbound) leg (CDP+2DS LWP=297 g m⁻²). d)-f): P2 ascent at 15.1
 461 UTC, 34.27°N, 73.65°W during outbound leg (LWP=526 g m⁻²). g)-i): P3 descent at 15.95 UTC, 33.91°N,
 462 73.07°W, on return (inbound) leg (LWP=400 g m⁻²). j)-l): P4 ascent at 15.8 UTC, 33.36°N, 72.80°W, on return
 463 leg (LWP=95 g m⁻²). Same labeling conventions as in Fig. 6. LWPs based on corrected CDP data.

464 Cloud top temperatures are consistently near $-10\text{ }^{\circ}\text{C}$ throughout the flight (Fig. 12), despite cloud
465 top heights simultaneously rising to over 2.5 km, the highest of the five flight days. This indicates
466 a warming boundary layer with fetch. Five dropsondes, straddling the GS within 350 km of each
467 other, detail the evolution of the boundary layer (Fig. 13). Furthest west, a well-mixed clear-air
468 boundary layer of one km depth and a potential temperature (θ) of 276 K overlaid an SST of \sim
469 286 K (Fig. 2). The spatially-subsequent sounding (orange line), \sim 120 km further east over the
470 Gulf Stream, also sampled a mostly well-mixed lower boundary layer now warmed to a θ of \sim
471 278 K. The SSTs have increased more, however, reaching 290 K, so that the air-sea temperature
472 difference has increased to 12 K. The inversion height has increased only slightly, to \sim 2 km.
473 East of the dropsonde, rimed ice was already sampled during the first ACB leg, in thin cloud at a
474 temperature of $-6.6\text{ }^{\circ}\text{C}$ (Fig. 12b, 14.81 UTC) for which the leg-mean N_d exceeded 600 cm^{-3} . An
475 interesting feature is a further increase in θ by \sim 1 K within the lowest 200 m, despite the presence
476 of snow (2DS image at 15.10 UTC in Fig. 12b). The precipitation habit in the nearby MinAlt
477 leg (Fig. 12c) is melting snow and liquid, at $3\text{ }^{\circ}\text{C}$, for a leg-mean rainrate of 0.26 mm hr^{-1} . The
478 near-surface θ increases suggests the thermal fluxes off of the ocean are strong enough to override
479 any evaporation-induced cooling. Winds above the capping inversion shift to almost southerly,
480 increasing the ability for shear to induce entrainment.

481 The dropsonde at the eastern GS edge (green line), is associated with near-surface rainrates of
482 $\sim 0.35\text{ mm hr}^{-1}$ (Fig. 12b), yet the lower boundary layer has warmed further to a θ of 280 K in
483 the lowest one km, with the capping inversion slightly raised to 2.1 km. This profile too shows
484 a distinct warming in the lowest 100 m near the surface, if less pronounced. The subsequent
485 profile (red line), taken on the outbound flight just before the transition to open-celled convection,
486 sampled a more stabilized cloudy boundary layer that had deepened to approximately 2.5 km and
487 incorporated a lower-tropospheric moist layer. The sub-cloud θ has warmed to 282 K. Within the
488 lowest 400 m, a cooling indicative of rain evaporation is now present. This dropsonde is close to
489 open-celled cloud structures further east. The furthest east dropsonde, east of the GS, fell within
490 the open-celled convection, within a well-mixed boundary layer with a θ of 285 K reaching 1.5
491 km, and twice the specific humidity of the initial sounding. The air-sea temperature differences are
492 still significant at 9 K, but combined with slightly diminished near-surface wind speeds of 10-12
493 m s^{-1} , the buoyancy fluxes have reduced to $< 200\text{ W m}^{-2}$ (Fig. 2).

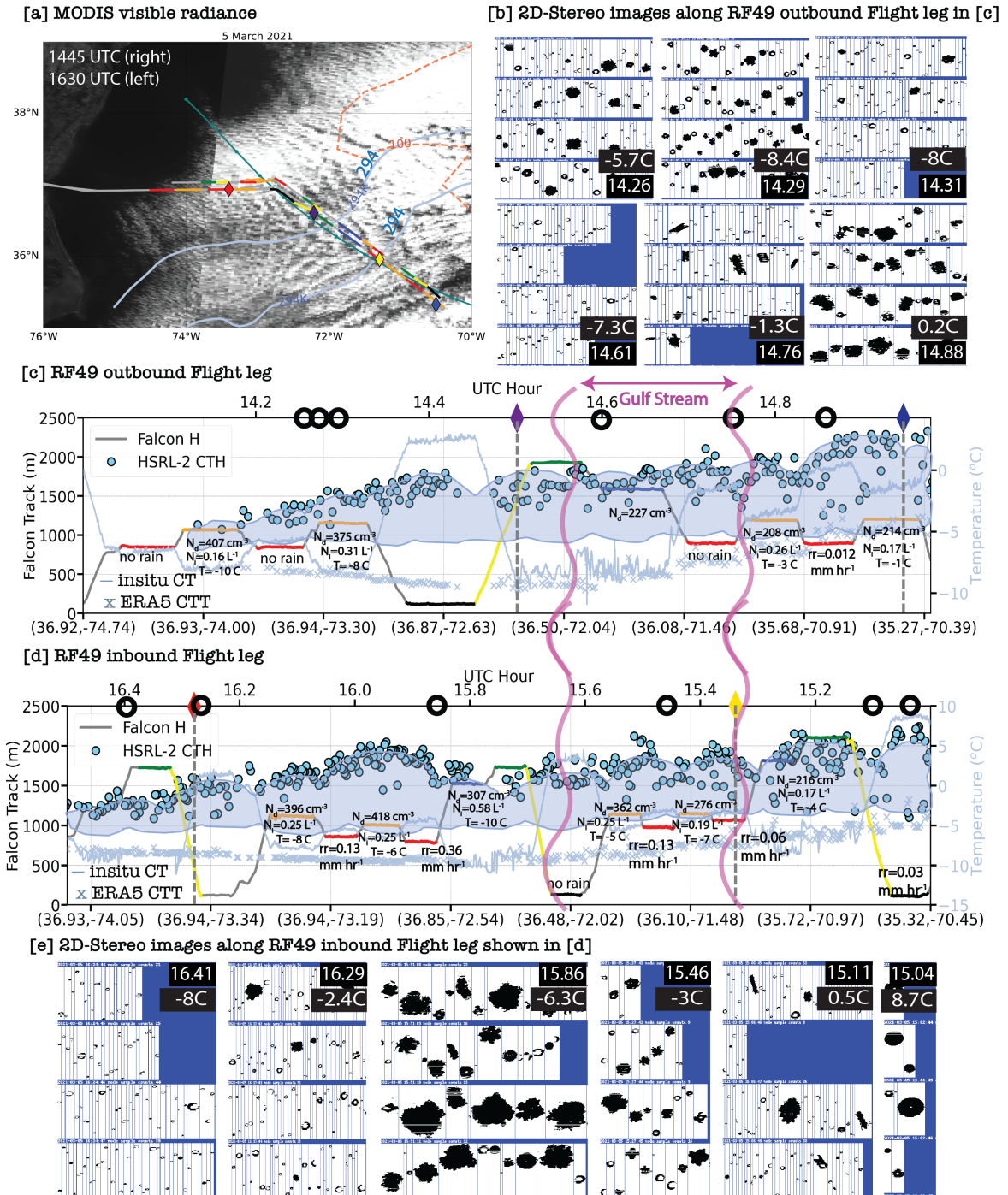
494 The dropsondes reveal that the 0 °C level increases from approximately 0.5 km to 1.2 km over
495 a distance of ~ 350 km (Fig. 13a). At the same time, the cloud base height descends throughout
496 the eastward evolution (see ACB legs in Fig. 12). The cloud base temperatures increase from ~ -4
497 °C at the western GS edge to ~ 3 °C at the eastern GS edge (Table S1). Near-surface precipitation
498 quickly transitions to liquid, and is certainly liquid by the time the cloud deck transitions to an
499 open-celled morphology, with ice columns and snow aggregates still present in the overlying cloud
500 (Fig. 12d, 2DS imagery at 15.82 UTC and 16.03 UTC, as well as at 14.95 and 15.10 UTC). This
501 has implications for surface cold pools, as the fall speeds of rain exceed those for snow, so that more
502 evaporation is likely to occur closer to the surface. Precipitation increases to the east, reaching
503 above 0.5 mm hr⁻¹ near the surface at 15.4 UTC, just prior to the transition to a more open-celled
504 cloud morphology, and a surface cold pool is present in the nearby sounding (red dropsonde in
505 Fig. 13b).

506 The four *in situ* profiles also show the boundary layer deepening, coupled with a rising 0 °C level
507 (Fig. 14). Snow/ice particles remain to temperatures of ~ 3 °C. N_i are higher in the thicker cloud,
508 with ice columns, graupel and supercooled liquid drops present within the HM temperature regime
509 (or warmer, possibly advected in from above). In contrast to the CAO from four days previous,
510 the HM mechanism may be effective in producing ice on this day. The highest N_i occurs where
511 drizzle is most plentiful in furthestmost east profile at 15.1 UTC (Fig. 14, bottom row). Droplet
512 shattering likely remains an ineffective SIP mechanism, as the *in situ* r_e near cloud top are 10 μ m
513 or lower, matched well by the RSP-retrieved r_e (Fig. A4c). N_i increase with IWC in the ACB level
514 legs (not shown) suggesting collisional breakup can also contribute to the N_i . The RSP retrievals
515 indicate a small but consistent increase in cloud-top r_e with distance offshore (Fig. A4c), while the
516 RSP-derived LWP of 400 g m⁻² on the outbound leg increases over the thickest stratiform segment
517 to LWPs over 600 g m⁻².

518 *d. 5 March 2021*

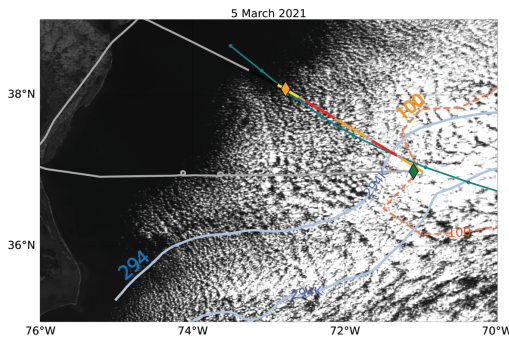
519 By 5 March 2021, warmer Gulf Stream waters extended further to the northeast (Fig. 2), and
520 a narrowly-defined GS with buoyancy fluxes reaching 400 W m⁻² was fully transected by both
521 planes during the morning (RF49; Fig. 15), with the afternoon RF50 only reaching the middle of
522 the GS (Fig. 16). Near-surface wind speeds reach 12 m s⁻¹, MODIS LWPs reach 100 g m⁻², and

523 maximum leg-mean N_d are near 500 cm^{-3} . These values are all lower than the maxima from 3
524 February 2021. The dropsonde profiles (7 total, Fig. S3) show a well-mixed boundary layer at the
525 furthest west (19.82 UTC) initially capped at $\sim 1.4 \text{ km}$, deepening to $\sim 2.2 \text{ km}$ by the eastern end.
526 Cloud tops rise by $\sim 200 \text{ m}$ per degree, with T_{ct} cooling slightly from $\sim -8 \text{ }^\circ\text{C}$ to a minimum of -10
527 $^\circ\text{C}$.

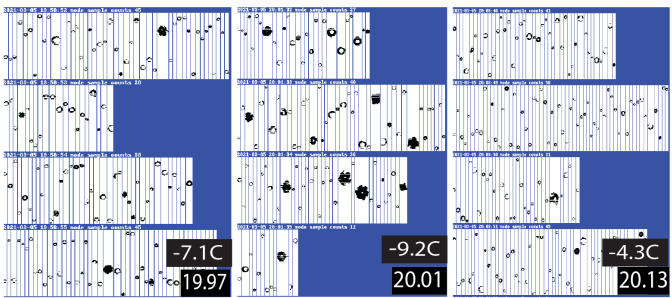


528 FIG. 15. 5 March 2021 morning (Rf49). Similar notation to Fig. 5. First and third ascent partial profiles upon
529 return shown in Fig. S6.

[a] MODIS visible radiance



[b] 2D-Stereo images along Rf50 along-wind Flight leg in [c]



[c] Rf50 along-wind Flight leg

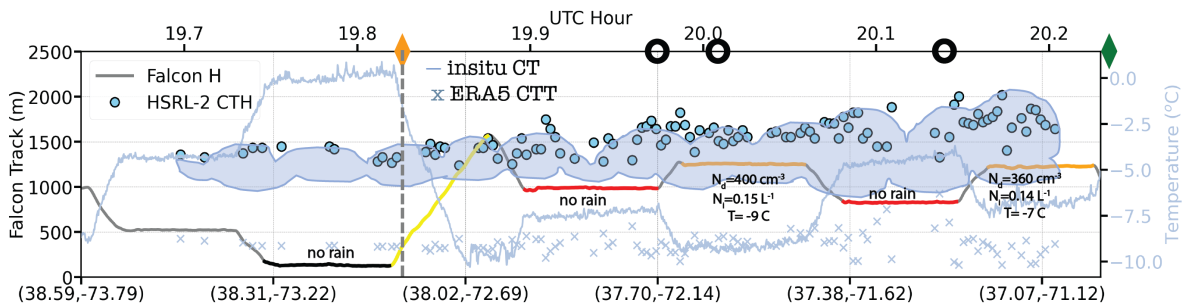


FIG. 16. 5 March 2021 afternoon (RF50). Same conventions as in Fig. 5.

530 The furthestmost east dropsonde crosses 0 °C at 1.1 km, with a cloud base temperature -4 °C.
531 Most particles near the melting level are ice (Fig. 15b at 14.88 UTC). Some light rain occurs near
532 the surface at the eastern end of the morning flight (Fig. 15e at 15.04 UTC). During the afternoon
533 flight (Fig. 16), the thin clouds were all primarily composed of liquid cloud droplets, and no
534 precipitation was detected.

535 Rimed ice particles are encountered on the first ACB legs (14.25 UTC within Fig. 15b and 19.99
536 UTC within Fig. 16b) of both flights, at *in situ* temperatures of -6 to -7 °C, within thin clouds with a
537 minimum T_{ct} near -8 °C. The high concentration of small super-cooled water droplets again suggests
538 primary ice production is likely occurring at the same time as the cloud initiation. 2DS imagery
539 throughout depicts super-cooled liquid water droplets and occasional large rimed ice particles and
540 snow aggregates (e.g. at 14.75, 15.11 and 15.46 UTC) with no clear indication of diffusional
541 growth. The highest N_i of 0.58 L⁻¹ is sampled during a BCT leg at 15.8 UTC at a temperature
542 of -10 °C. This implies a non-HM riming-splintering SIP mechanism. Rainrates remain light (0.1
543 mm hr⁻¹ at best), and the significant cloud deepening to the east suggests the reduction in N_d is
544 primarily occurring through cloud-top entrainment, rather than precipitation. MODIS imagery
545 does not clearly suggest an open-celled structure at the end of either flight (Fig. 2), suggesting the
546 transition to a lower-albedo cloud structure is primarily through continuing entrainment of warmer,
547 drier air, with weakening surface boundary fluxes (Fig. 2) less able to couple the surface to the
548 cloud layer.

549 *e. 8 March 2021*

550 Both planes traverse a narrower Gulf Stream three days later on 8 March 2021, during an
551 afternoon-only flight (RF51). After transecting the Gulf Stream, the planes headed south-southwest
552 to sample an area with broken clouds (Fig. 17). Near-surface winds are lighter (ERA5 wind speed
553 maxima of 8 m s⁻¹) and buoyancy flux maxima remain < 400 W m⁻² (Fig. 2). In contrast to the
554 other flights, clouds do not develop until the boundary layer flow reaches the eastern GS edge and
555 MODIS LWPs remain below 50 g m⁻² in the area sampled by the planes.

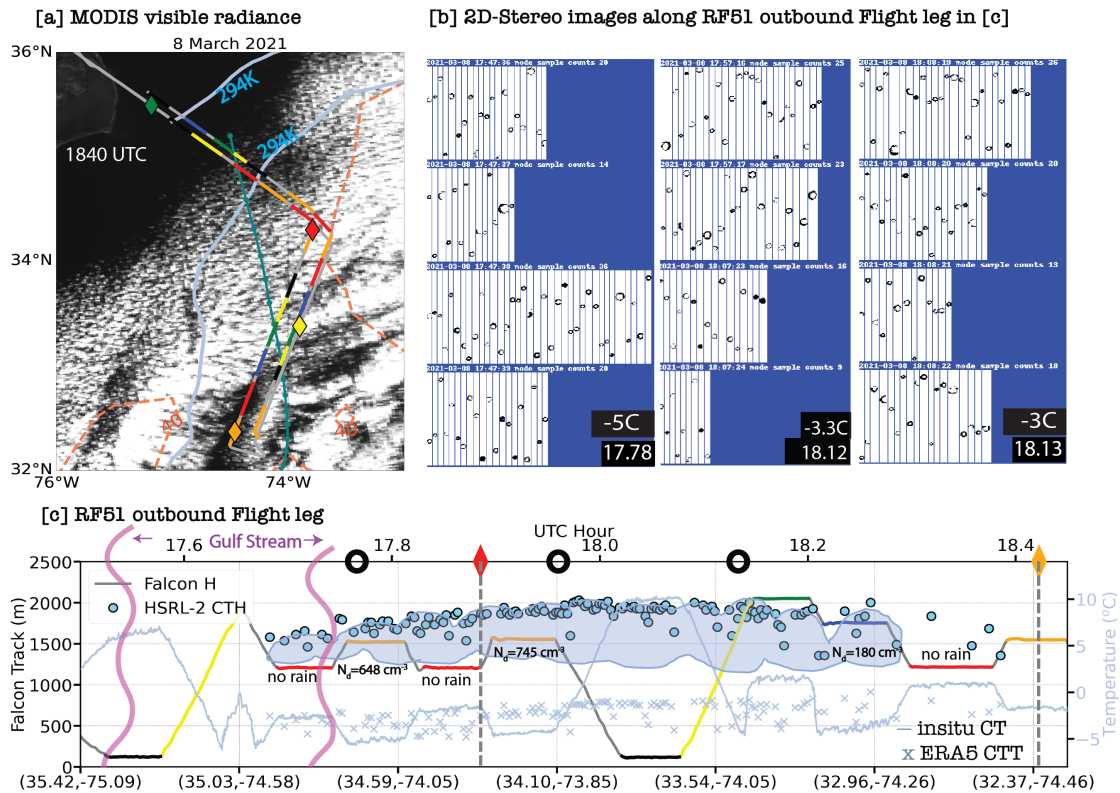
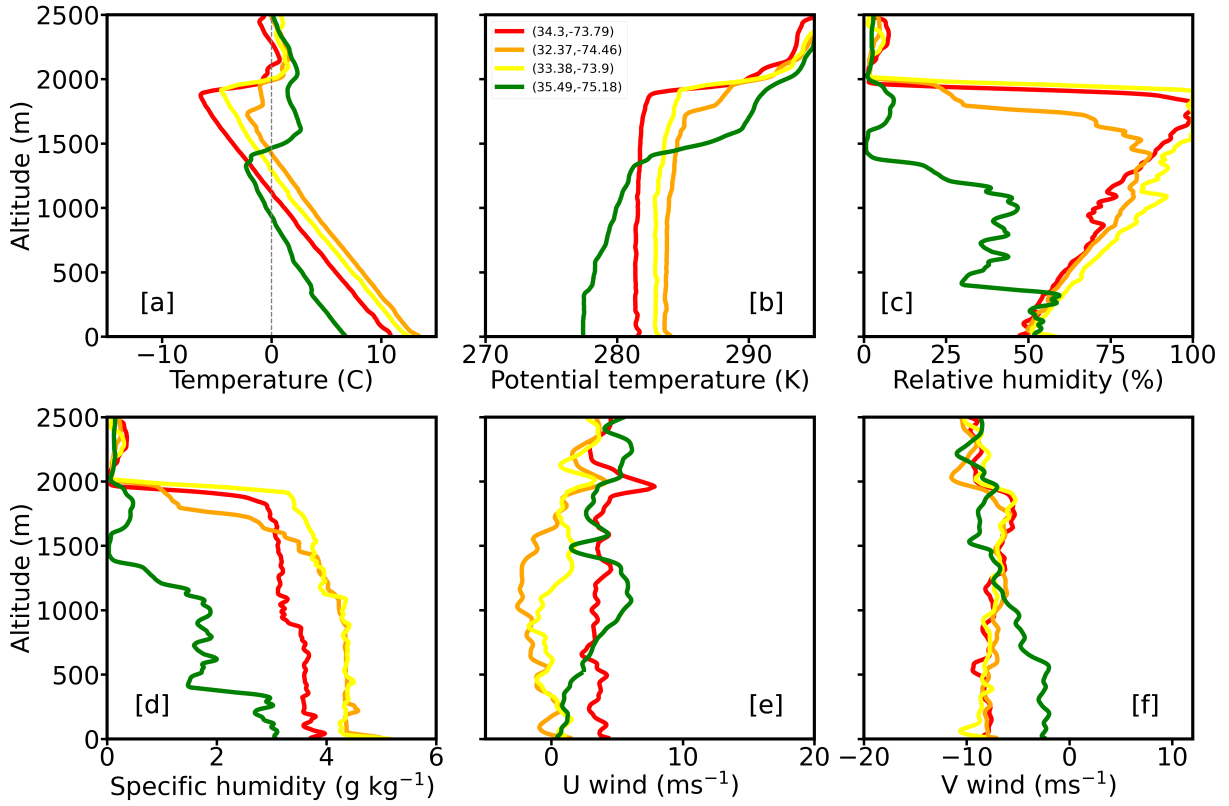


FIG. 17. 8 March 2021 afternoon flight (RF51). Ascent profiles shown in Fig. S7.



556 FIG. 18. 8 March 2021 (RF51) dropsonde profiles of a) temperature, b) potential temperature, c) relative
 557 humidity, d) specific humidity, e) zonal wind and f) meridional winds. Colors follow those indicated within
 558 diamonds in Fig. 17.

559 The dropsondes indicate the 0 °C level is already above one km at the western end of the flight
560 before the clouds develop, under a capping temperature inversion at ~ 1.3 km (Fig. 18). The
561 temperature inversion base deepens to near 2 km east of the Gulf Stream, and the 0 °C level and
562 cloud base rise to between 1.1-1.5 km. No precipitation is detected below cloud base anywhere,
563 indicating the ~50% reduction in N_d with fetch is primarily through cloud top entrainment. The
564 coldest cloud temperatures only reach -5 °C. No particles were deemed aspherical enough to qualify
565 as ice (see Fig. S5). However, on closer inspection, small mostly-spherical rimed ice particles are
566 evident in the 2DS imagery at 18.12 and 18.13 UTC (Fig. 17b). The lidar ratio at 532 nm also
567 indicates the presence of some ice. Ice particles have been detected at temperatures > -5 °C over
568 the southern oceans (Zaremba et al. 2021), with this case suggesting ice in such warm conditions
569 can also occur in these CAOs.

570 A roll circulation is suggested by the MODIS visible imagery, although the wind shear expected
571 for a roll circulation (e.g., Young et al. 2002) is not present (Fig. 18d and e). Two dropsondes are
572 located near each other, one within the clear area and the other sampling a nearby cloud (orange
573 and yellow in Fig. 18). These have similar boundary layer specific humidities, with the clear-sky
574 sounding being ~ 1 °C warmer, capped by a slightly lower inversion height than its neighbor. The
575 buoyancy fluxes are also weaker (Fig. 2). Surface relative humidities remain near 50% for all four
576 dropsondes, and the fluxes and updrafts may simply be too weak (Fig. 4) to bring near-surface
577 air to its lifting condensation level, within the clear region. Mesoscale descent could additionally
578 be acting to help dry and warm the cloud layer, as suggested for some CAOs within Chou and
579 Ferguson (1991), and lower the inversion height. The cloud organization apparent in the visible
580 imagery suggests this could be occurring, but this remains speculative without further analysis.

581 **5. Evidence for Primary and Secondary ice production**

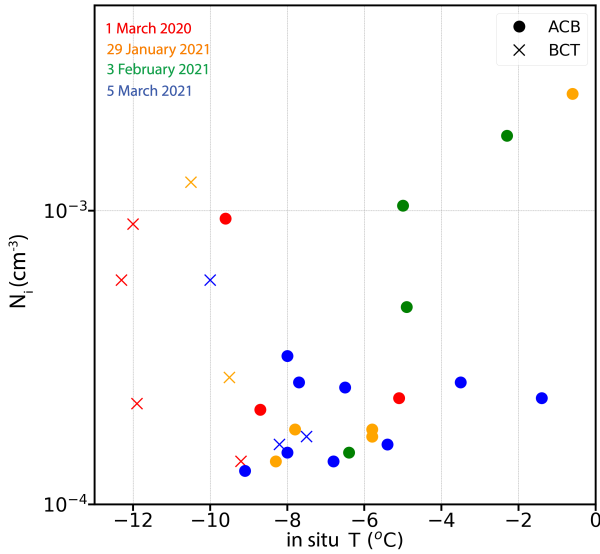
582 Ice particles detected at the first pass through thin, developing cloud, just downstream of clear
583 skies, in four of the examined cases indicates primary ice nucleation occurring at temperatures
584 between -4 °C to -8 °C. This nucleation may be aided by strong updrafts. Marine boundary
585 layer INP concentrations measured off the coast of eastern Nova Scotia ranged from 10^{-4} to
586 10^{-3} cm⁻³ (Irish et al. 2019; Welti et al. 2020). These exceed measured marine-originating INP
587 concentrations over the Southern Oceans (McCluskey et al. 2018) and globally (DeMott et al.

588 2016), by 2-3 orders of magnitude at -15 °C. Electron microscopy identified the northwest Atlantic
589 INP as mineral dust (Irish et al. 2019). INP concentrations during ACTIVATE CAOs can well be
590 similarly elevated by outflow of continental soil aerosols. Welti et al. (2020) suggest the following
591 estimate of primary ice nuclei concentrations based on a best-fit to multiple measurement datasets:
592 $INP=(T+5)*(-10^{-5}*\exp(500/T+60))$ with T in Celsius and INP in m^{-3} . This equation estimates an
593 INP concentration of $1.1*10^{-3} L^{-1}$ at -10 °C, reducing to zero at -5 °C.

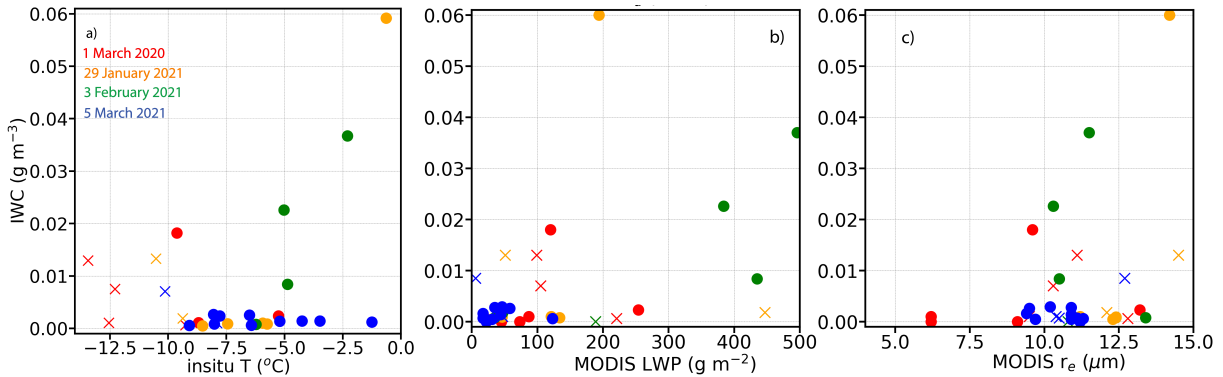
594 The empirical Welti et al. (2020) INP estimate is 1-2 orders of magnitude less than that in
595 currently used parameterizations of INP. At -10 °C, the Meyers et al. (1997) contact nucleation
596 formulation estimates INP of $0.3 L^{-1}$. The deposition freezing parameterization of Cooper (1986)
597 produces an INP estimate of $0.05 L^{-1}$. The immersion freezing parameterization of Bigg (1953)
598 produces lower concentrations, but overall, these parameterizations overestimate INPs relative to
599 Welti et al. (2020). The parameterization overestimate is consistent with the known bias in cloud
600 phase within global models, wherein ice depletes super-cooled water too quickly (e.g., Atlas et al.
601 2022).

602 Nevertheless, ice particle concentrations measured during the ACTIVATE CAOs cannot be
603 explained by primary ice production alone. We compile the ice microphysical properties for the
604 four ice-containing flights in Figs. 19-21 to help identify dominant production mechanisms for
605 secondary ice production. *In-situ* temperatures of the ACB and BCT legs range between -12 °C
606 to near 0 °C, with most occurring between -5 °C to -9 °C (Fig. 19). Measured N_i concentrations
607 range from $0.1 L^{-1}$ to $5 L^{-1}$, with the larger values found both near colder cloud tops (< -8 °C)
608 and warmer ACB legs (Fig. 19). The N_i enhancement is consistent with other observations within
609 convective clouds with cloud top temperatures warmer than -12 °C (Abel et al. 2017; Field et al.
610 2017; Järvinen et al. 2022). Notably, although many of the elevated N_i values fall within the HM
611 temperature regime (-3 °C to -8 °C), the highest N_i concentrations mostly occur at either warmer
612 or colder temperatures.

620 The distribution of IWC with temperature is also bimodal (Fig. 20a). IWCs are also higher for
621 larger LWPs and larger cloud-top effective radius (both from MODIS; Fig. 20b and c), with a less
622 clear relationship to the *in situ* r_e or temperature (not shown). The colder cloud tops correspond
623 to thicker clouds with more liquid water (Fig. S8), and the highest ice water contents occur within
624 the clouds with the coldest tops (Fig. S9). These reach temperatures that favor dendritic vapor-



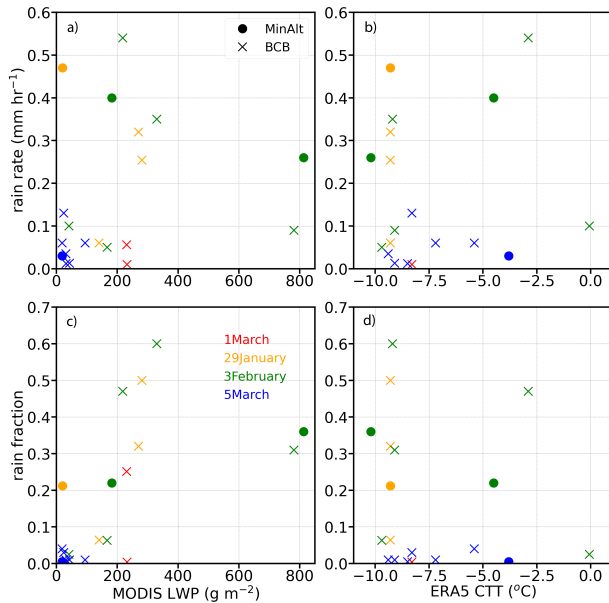
613 FIG. 19. Leg-mean *in-situ* N_i (one-second values > 0 only) versus temperature for the ACB (filled circles) and
 614 BCT (crosses) aircraft legs.



615 FIG. 20. Leg-mean *in-situ* IWC versus a) *in-situ* temperature, b) MODIS-derived LWP and c) effective radius
 616 (r_e), for above-cloud-base (ACB, filled circle) and below-cloud-top (BCT, crosses) aircraft legs. One-second
 617 N_i values > 0 only.

625 diffusional growth whose slower particle fall speeds allow more time for particle growth, also seen
 626 in the sub-Arctic (Chellini et al. 2022). Rainrates and rain fractions are larger for higher LWPs and
 627 colder T_{ct} s (Fig. 21).

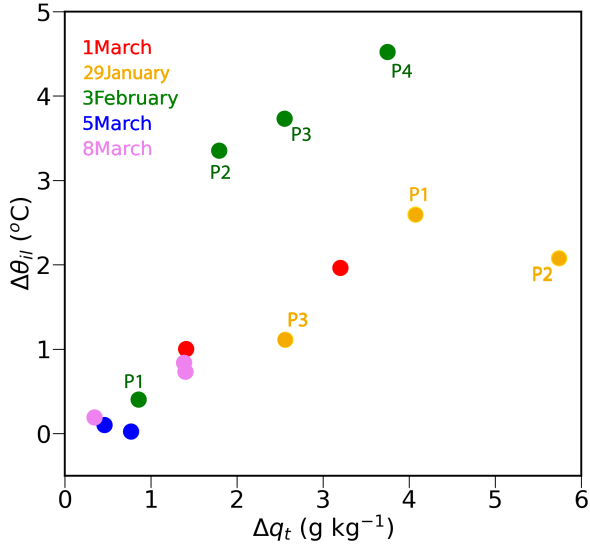
628 The ice habits associated with the best-known SIP mechanism, riming followed by ice splintering
 629 at temperatures between -8 °C and -3 °C (Hallett and Mossop 1974), are columns, super-cooled
 630 liquid drops, and rimed particles are all evident within 2DS imagery for the 3 February 2021 case.



618 FIG. 21. *in situ* leg-mean rain rates versus a) MODIS LWP, b) ERA5 T_{ct} ; leg-mean *in situ* rain fractions versus
 619 c) MODIS LWP and d) ERA5 T_{ct} . Rain rates and fractions based on one-second rain rates $> 0.01 \text{ mm hr}^{-1}$ only.

631 The HM mechanism is common in CAOs in the sub-Arctic region (Abel et al. 2017; Mages et al.
 632 2023) and the southern oceans (Järvinen et al. 2022). That said, HM production of small ice
 633 columns is not always evident, notably within the strongest CAO occurring on 29 January, 2021.
 634 Instead, the largest N_i occur outside the HM temperature range (Fig. 19), and are often associated
 635 with higher IWCs. This suggests fragmentation after ice-ice particle collision, of either dendrites
 636 and/or graupel, is the more dominant SIP form. The graupel particles vary in size, which will
 637 also vary their fall speeds, a requirement for particle collisions. Ice-ice collisions generate ice
 638 splinters most effectively at temperatures $\sim -16 \text{ }^\circ\text{C}$ (Takahashi et al. 1995), aided by the more
 639 fractal surfaces such as the snowflakes evident on 1 March 2020. Cloud top temperatures almost
 640 reach this temperature regime during the more intense CAOs (29 January and 3 February 2021).
 641 Positive correlations between N_i and IWC, such as on 29 January 2021 (Fig. 11), also occur on 1
 642 March 2020 and 3 February 2021.

643 Because of the strength of the surface fluxes, 1 Hz updraft velocities at cloud base can easily
 644 reach 5 m s^{-1} (Fig. 4), in line with Mages et al. (2023). Closer to cloud top, the updrafts may also be
 645 able to bring some liquid droplets above the existing inversion, where they form an additional, thin,
 646 stratiform cloud layer under a new inversion, though horizontal inhomogeneities in cloud top height



663 FIG. 22. Boundary layer decoupling metrics $\Delta\theta_{il}$ vs Δq_t . Profile labeling corresponds to that in Figs. 9-12 and
 664 Fig. 14.

647 can also explain this observation. A growing body of work is indicating that SIP is more likely to
 648 occur within updrafts (Luke et al. 2021; Mages et al. 2023), although a cursory examination did
 649 not reveal this for the cases examined here. This could be because the up/downdrafts also facilitate
 650 a recirculation of ice, constituting an internal feeder-seeder process. Deep strong updrafts are
 651 capable of lofting both graupel and generating super-cooled liquid droplets, and SIP is preferred
 652 near cloud top when both graupel and super-cooled liquid are present. Recirculation of ice may
 653 also facilitate a synergism across different SIP mechanisms (Sotiropoulou et al. 2020).

654 The strong updrafts, by increasing N_d and keeping drop sizes small, discourage attribution to the
 655 SIP mechanisms of droplet freezing and fragmentation during sublimation. Droplet fragmentation
 656 upon freezing (drop-shattering) is more effective for droplets with diameters $> 100 \mu\text{m}$ (Korolev
 657 et al. 2020; Luke et al. 2021) and drizzle drops are few at the colder T_{ct} . High supersaturation within
 658 strong updrafts can also enhance INP activation. This may be occurring, but cloud temperatures
 659 are too warm for significant primary ice particle production. Fragmentation through sublimation
 660 also seems unlikely because the large number of super-cooled droplets will maintain a relative
 661 humidity near water-saturation.

662 *a. Is precipitation-induced decoupling occurring?*

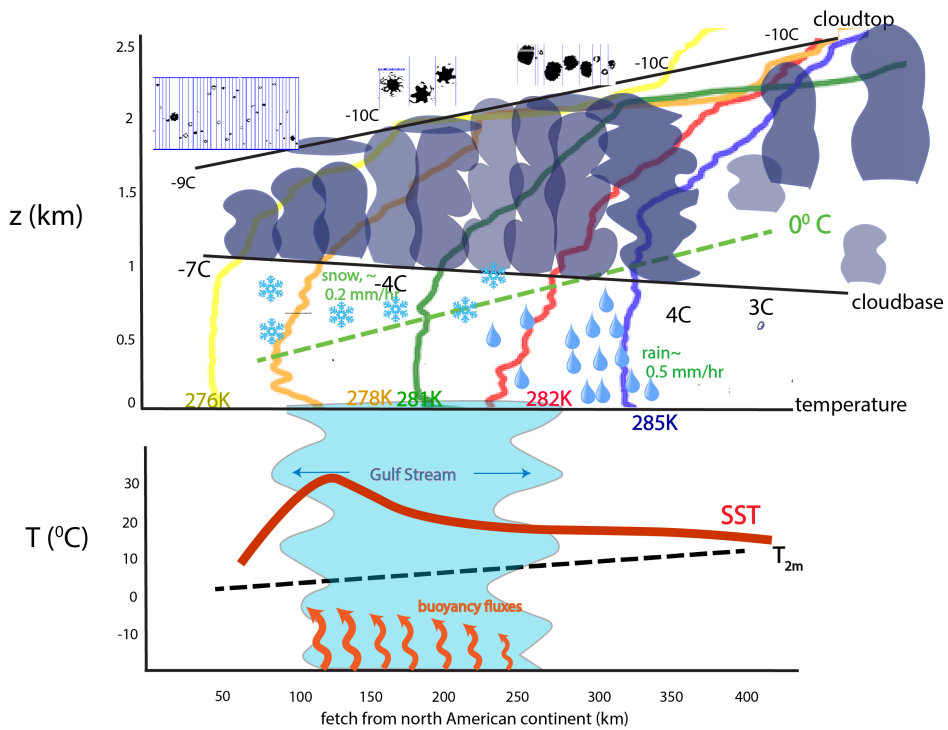
665 Precipitation-induced decoupling is generally necessary to the transition to open-celled structures
666 in subtropical marine stratocumulus (Wood et al. 2011), and is emphasized within Abel et al.
667 (2017) for a sub-Arctic CAO cloud transition. We investigate boundary layer decoupling for the
668 ACTIVATE CAOs using the metric developed within Jones et al. (2011), also applied within Abel
669 et al. (2017). Differences between the upper ("top") and lower ("bottom") quarter of the boundary
670 layer total water (ice+liquid+vapor mixing ratio; q_t) and the ice-liquid water potential temperature
671 (θ_{il}) indicate the degree to which the cloud and sub-cloud layers are coupled. Profiles with Δq_t (=
672 $q_{t,bottom} - q_{t,top}$) of 1.5 g kg^{-1} and $\Delta\theta_{il}$ (= $\Delta\theta_{il,top} - \theta_{il,bottom}$) of $\simeq 1 \text{ }^\circ\text{C}$ in Fig. 22 are considered
673 well-mixed. These apply primarily to 5 and 8 March 2021 and the most western profiles from
674 1 March 2020 and 3 February 2021. This further supports the idea that the CAO cloud fraction
675 on 5 and 8 March 2021 eventually becomes reduced because buoyancy fluxes become too weak
676 to support a cloudy boundary layer. Many of the other profiles possess more dramatic vertical
677 gradients in q_t and θ_{il} than does the Abel et al. (2017) CAO, especially further east. The boundary
678 layer on 3 February, which supports the largest rain rates and fractions of the 5 days, is the deepest
679 and most decoupled in temperature. Precipitation is closely linked to decoupling for both 29
680 January and 3 February 2021. Thus although surface fluxes may overcome rain-induced cooling
681 near the surface in places (e.g., Fig. 13), the lower quarter of the boundary layer is still only
682 occasionally coupled to the cloud layer though cumulus. Interestingly, despite being decoupled, all
683 of the 29 January 2021 profiles still correspond to overcast conditions, as does the P3 3 February
684 2021 profile. This is consistent with detrainment near cloud-top and serves to demonstrate how the
685 bottom-up convection of cold-air outbreaks underneath a synoptically-induced inversion influences
686 cloud fraction differently from the subtropical cloud decks.

687 **6. Conclusions**

688 As outbreaks of cold air flow off of the eastern north American continent in the boreal winter
689 and spring over the cold Labrador current, and then over the warm Gulf Stream, strong surface
690 fluxes of heat and moisture deepen the boundary layer, saturate its upper level with moisture and
691 foster significant cloud development, over a distance of under 1000 km. The surface fluxes typically
692 initiate cloud near the western edge of the Gulf Stream at $< 0 \text{ }^\circ\text{C}$ temperatures, developing reflective

693 stratiform cloud decks that devolve into lower-albedo cloud structures as the flow moves past the
694 eastern GS edge. Cloud tops rise to mostly remain at their initial temperature, ranging between
695 $-10\text{ }^{\circ}\text{C}$ to $-14\text{ }^{\circ}\text{C}$ for the more intense CAOs, while the $0\text{ }^{\circ}\text{C}$ level rises more dramatically, so that
696 more and more of the cloud comes to occupy temperatures $> 0^{\circ}\text{C}$.

697 The transition to lower-albedo cloud can occur via two pathways. In the five days examined
698 here, the more intense CAOs, which typically occur earlier in the year (Painemal et al. 2023),
699 deepen more and sustain both more ice and more rain by the eastern GS edge, than do the less
700 intense CAOs occurring later in the year. In the limited sample size examined here, precipitation
701 reaching the surface only sets in after the CAO has reached the eastern GS edge and beyond. Since
702 super-cooled liquid exists throughout the vertical column, the precipitation reaching the surface
703 could either be from melting snow or the collision-coalescence of liquid droplets. The presence
704 of strong updrafts suggests graupel is likely the common precursor to the rain, however, consistent
705 with space-based radar and lidar analysis (Field and Heymsfield 2015; Mülmenstadt et al. 2015).
706 The rain facilitates the transition of the more intense CAOs (29 January and 3 February, 2021) to
707 an open-celled organization. More intense CAOs are known to produce more extended high cloud
708 fractions (Fletcher et al. 2016), and the high aerosol loadings should maintain the stratiform decks
709 for longer (Murray-Watson et al. 2023), as is also observed in the satellite imagery shown here.
710 In this study, thin cloud layers may be occurring above well-defined inversion bases (e.g., Fig. 6),
711 because of the strong updrafts, though the layers may also correspond to detrainment from cloud
712 tops at different heights. The cloud deepening and N_d depletion lag the SST increase (Tornow et al.
713 2021). These processes are encapsulated in Fig. 23. In the second pathway, the cloud breakup
714 for the weaker CAOs (5 and 8 March 2021) is better explained by surface fluxes that become too
715 weak to sustain cloud development within deeper boundary layers that have warmed with fetch.
716 Mesoscale wind circulations generated either by the strong SST gradients (Small et al. 2008; Liu
717 et al. 2014) or above-cloud-top wind shear (Young et al. 2002) may potentially impose imprints
718 on the cloud organization, but this remains a topic for future research. We also note that for
719 this regime, LWP and N_d are not anti-correlated as they are for other suppressed marine regions
720 (Gryspeerdt et al. 2019).



721 FIG. 23. Schematic depiction of main processes controlling the microphysical evolution of cold-air outbreaks
 722 over the northwest Atlantic, including the dropsonde profiles of potential temperature from 3 February 2021.

723 Ice is already present even in thin, polluted clouds with small drops for which T_{ct} barely reaches
724 $-5\text{ }^{\circ}\text{C}$ - $-8\text{ }^{\circ}\text{C}$, even for the weakest, warmest, CAO. The proximity to clear-sky region upwind
725 suggests that the primary ice nucleation occurs at the time of cloud initiation. We hypothesize
726 the land-originating aerosol composition emanating off of the eastern seaboard already contains
727 some ice-nucleating particles, similar to measurements above Baffin Bay (Irish et al. 2019), though
728 marine emissions are also a possibility. Thereafter, rimed ice co-exists with small supercooled
729 liquid drops, aided by updrafts reaching five m s^{-1} . In temperature ranges that favor dendritic
730 growth, snowflakes are also apparent (e.g. 1 March 2020). Elevated ice number concentrations,
731 outside of the Hallett-Mossop temperature range, contribute to a growing body of evidence for
732 other SIP mechanisms at temperatures warmer than $-15\text{ }^{\circ}\text{C}$ (Zaremba et al. 2021; Järvinen et al.
733 2022). N_i are highest near cloud top and near cloud base and correlate with IWC for the three
734 more intense CAOs. Elevated IWCs near $0\text{ }^{\circ}\text{C}$ indicates enhanced ice aggregation. Although
735 the 2DS imagery is not definitive, ice-ice (including graupel) collisions, favored in temperature
736 ranges that support dendritic growth and enhanced ice aggregation, is hypothesized to produce the
737 secondary ice. SIP occurs outside the HM temperature range on 29 January 2021, while four days
738 later on 3 February 2021, HM rime-splintering is evident in ice columns. This suggests multiple
739 SIP pathways can readily occur, similar to the sub-Arctic (Sotiropoulou et al. 2020; Karalis et al.
740 2022) and over the southern Oceans (Järvinen et al. 2022; Atlas et al. 2022). Small droplets
741 should discourage droplet freezing, all else equal, with the strong up- and downdrafts facilitating
742 recirculation of ice that may further promote ice production.

743 The cold-air outbreaks examined here differ from those in the sub-Arctic and southern Ocean in
744 part by being more polluted (Dadashazar et al. 2021), increasing the N_d to values $> 500\text{ cm}^{-3}$ on
745 the western side of the Gulf Stream. In addition, the SST gradients are more pronounced than over
746 the sub-Arctic, supporting surface fluxes and updrafts that can reach above 500 W m^{-2} and five
747 m s^{-1} (contrast with surface fluxes and updrafts that remained below 200 W m^{-2} and two m s^{-1}
748 in Young et al. (2016), Abel et al. (2017) and Duschka et al. (2022)). Further work remains to be
749 done. Several of these cases lend themselves well to a follow-up study that can better differentiate
750 cause and effects. Dynamical effects from mesoscale circulations induced either by the strong
751 SST gradients and/or wind shear remain unexplored. In addition, a future study evaluating the full

752 dataset of available profiles will be required to better assess the various remote sensor retrievals in
753 these mixed-phase conditions.

754 *Acknowledgments.* We gratefully acknowledge funding support through grant 80NSSC19K0390
755 to University of Miami and grant no. 80NSSC19K0442 to University of Arizona. Christiane
756 Voigt and Simon Kirschler were funded by the Deutsche Forschungsgemeinschaft (DFG, German
757 Research Foundation – TRR 301 – Project ID 428312742 and SPP 1294 HALO under contract
758 no. VO 1504/79-1). We thank Kevin Sanchez and Alexei Korolev for their insights into cloud
759 probe behavior and microphysical behavior. The NASA Earth Venture Suborbital-3 Aerosol
760 Cloud meTeorology Interactions Ver the western ATlantic Experiment (ACTIVATE) campaign
761 was funded by NASA’s Earth Science Division and managed through the Earth System Science
762 Pathfinder Program Office.

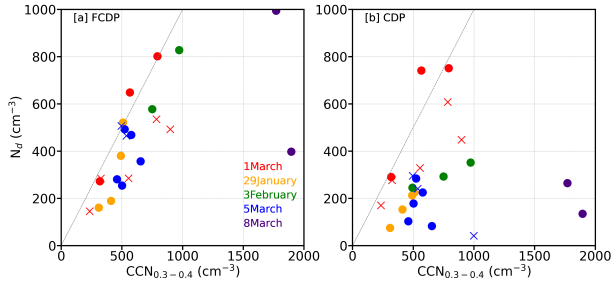
763 *Data availability statement.* All ACTIVATE datasets are available through ASDC: Atmo-
764 spheric Science Data Center [data set], [https://doi.org/10.5067/SUBORBITAL/ACTIVATE/](https://doi.org/10.5067/SUBORBITAL/ACTIVATE/DATA001)
765 [DATA001](https://doi.org/10.5067/SUBORBITAL/ACTIVATE/DATA001), 2020.

766 APPENDIX A

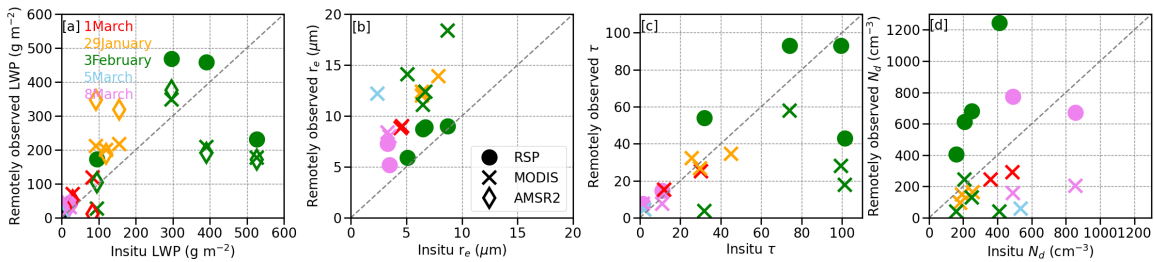
767 **Assessment of *in situ* and remotely-retrieved cloud properties**

768 A complete assessment of the ‘best-estimate’ N_d values from either the probes or the RSP
769 is beyond the scope of this work, but here we provide a preliminary analysis. CDP N_d values
770 are typically smaller than those from the FCDP, perhaps because of coincidence undercounting,
771 wherein two or more particles simultaneously travel through a sample volume but are counted as
772 one, and because of differences in the effective flow speed of $\sim 15\%$. The effective radius (r_e)
773 values are similar between the two probes for 2020 data, indicating the N_d difference is primarily
774 an undercounting at all sizes. An empirical correction based on 2020 data is applied: $N_{d,CDP_{corr}} =$
775 $\alpha (e^{(\beta * N_{d,CDP})} - 1)$, with $\alpha=1820$ and $\beta =6.9e-4$ (Kevin Sanchez, personal communication). This
776 closely follows the Lance (2012) correction. The corrected CDP N_d values exceed the FCDP
777 values on average in 2020 (mean ratio of 1.9), but are 70% of the FCDP values in 2021 on average.

778 Small changes in voltage can also dramatically change the number of droplets meeting the 3 μm
779 diameter threshold of the FCDP, however. The FCDP N_d concentrations are typically only slightly
780 less than the CCN concentrations measured at 0.3-0.4 % supersaturation (Fig. A1a) based on just
781 the data from the five investigated flight days. The CDP N_d values show a relationship to the CCN
782 that is more typical of marine environments. The FCDP N_d values, while high, are nevertheless



785 FIG. A1. Cloud droplet number concentrations (N_d) versus cloud condensation nuclei concentration (CCN)
 786 measured at 0.3-0.4% supersaturation, taken from level legs occurring below one km in altitude gridded to
 787 one-degree, for a) FCDP and b) the corrected CDP data.



797 FIG. A2. RSP (filled circles) and MODIS (crosses) retrievals versus *in-situ* values of a) LWP, includes
 798 microwave-derived AMSR2-diamond, b) cloud-top effective radius r_e , c) cloud optical depth τ , and d) cloud
 799 droplet number concentration N_d . Flight day is indicated by color. RSP data are screened for the presence of
 800 higher clouds.

783 possible for a regime with strong surface fluxes, and which may contain further aerosol capable of
 784 becoming activated at higher supersaturations.

788 The available remotely-retrieved (RSP, MODIS, and AMSR2) cloud properties are also compared
 789 to those calculated from the available *in situ* profiles, for both the FCDP probe (Fig. A2) and the
 790 CDP probe (Fig. A3), and, for the RSP, shown along the 3 February 2021 flight track with the CDP
 791 r_e values (Fig. A4). The RSP retrieves the r_e and cloud optical depth τ using multi-angle polarized
 792 radiances at the cloud bow, primarily at the 865 nm wavelength. The radiances are dominated
 793 by single scattering and little impacted by three-dimensional radiative transfer effects (Alexandrov
 794 et al. 2012, 2015). The field of view is 14 mrad, and the data are aggregated into a one-second
 795 resolution, corresponding to a ~ 100 m spatial resolution, oriented along the aircraft track, then
 796 averaged further into one-minute moving averages in Fig. A4.

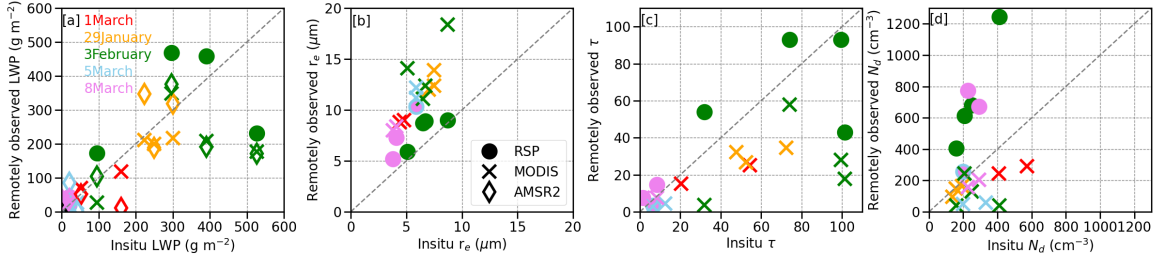
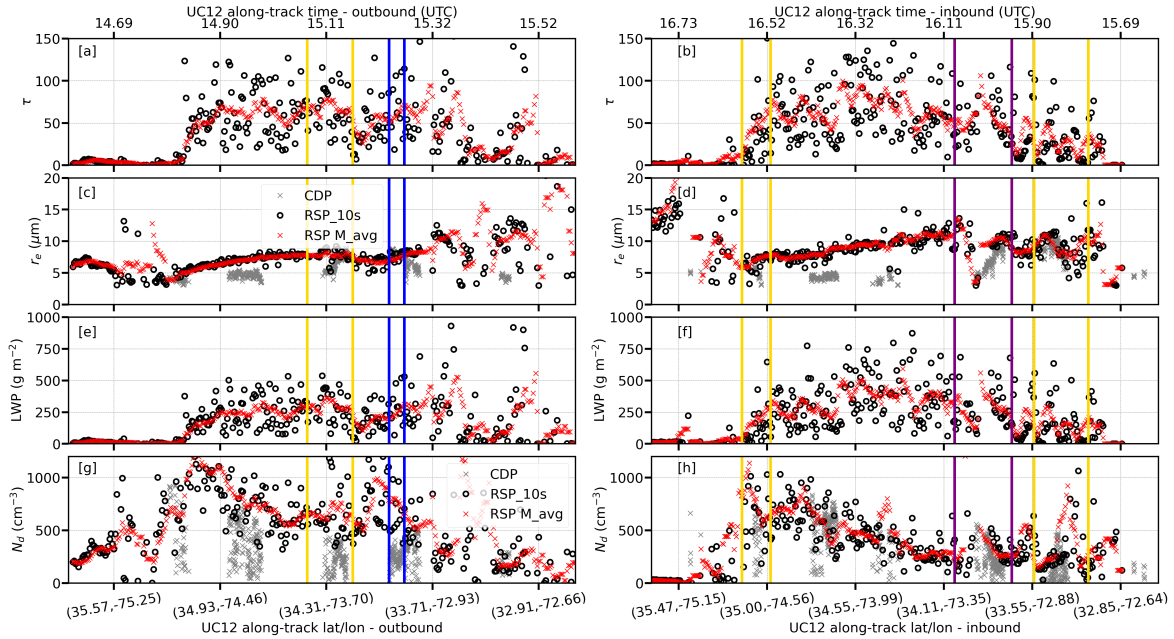


FIG. A3. similar to Fig. A1 but for the CDP probe values.



801 FIG. A4. a) RSP-derived cloud optical depths along outbound flight track of 3 February 2021 morning flight
 802 (RF44), from west to east, as ten-second and moving one-minute averages (black open circles and red asterisks,
 803 respectively). b) same as a) but for inbound (return) flight, west to east. c)-d): same as a)-b) but for RSP-derived
 804 r_e and that from the CDP probe where available (grey asterisks). e)-f): RSP-derived LWP. g)-h) RSP-derived
 805 N_d and that from the CDP probe where available (grey asterisks). Yellow/purple lines bracket ascent/descent
 806 profiles and dark blue indicates the BCT leg.

807 The RSP r_e is typically within two μm of the *in situ* values near cloud top, lending confidence
 808 to both measurements (Fig. A2b and Fig. A3b). In Fig. A4e-f, the RSP r_e slightly exceeds the
 809 *in situ* values from lower in the cloud, as expected. The strong correspondence between the RSP

810 and *in situ* cloud-top r_e is supported by a larger-scale assessment of ACTIVATE data (not shown),
811 comparisons to Langley CDP data over the northern Atlantic (Alexandrov et al. 2018), and from
812 another cloud probe over the southeast Atlantic (Adebiyi et al. 2020).

813 The *in-situ* τ values are summed over a profile of regridded, 20-m vertical-mean volume extinction
814 coefficients ($\beta(z)$) calculated from LWCs and effective radii ($r_e(z)$) as $\beta(z) = \frac{9LWC}{5\rho_w r_e(z)}$. The factor of
815 $\frac{9}{5}$ accounts for an adiabatic increase in LWC over the 20-m span, supported by the profiles. For the
816 six *in situ* profiles for which RSP retrievals are also available, the RSP cloud optical depths values
817 seem representative. LWP is estimated using $\frac{5}{9}\rho_w\tau r_e$, where r_e is the cloud-top value. Differences
818 from *in situ* LWP values are dominated by the differences in τ . RSP retrievals of N_d , calculated
819 using $N_d = k \frac{\tau^{0.5}}{r_e^{2.5}}$ with $k=1.4067 \times 10^{-6}$ [$\text{cm}^{-0.5}$] following Painemal and Zuidema (2011) typically
820 exceed vertically-averaged *in situ* values, similar to Gryspeerdt et al. (2022). This does reflect
821 vertical inhomogeneity in the *in situ* values in part. Along the 3 February 2021 flight track, the
822 RSP-derived N_d are close to the maximum *in situ* N_d values (Fig. A4g-h), reaching 1000 cm^{-3} in
823 places, while retrieved LWPs mostly remain 500 g m^{-2} . These comparisons tend to support each
824 other.

825 MODIS r_e values, retrieved at $3.7 \mu\text{m}$, typically exceed *in situ* values (see also Fig. S7),
826 consistent with other comparisons (e.g., Painemal and Zuidema 2011; Painemal et al. 2021).
827 MODIS τ estimates are consistently less than *in situ* values, likely because of unaccounted-for
828 horizontal photon transport (Zuidema and Evans 1998). The MODIS biases in τ and r_e somewhat
829 compensate each other within the LWP estimate, but nevertheless remain less than RSP-derived
830 LWPs (Figs. A2a-A3a). This is in large part due to the resolution difference between RSP and
831 MODIS (100 m versus 1 km). When RSP radiances are averaged, using a one-minute moving
832 average which gives a spatial average similar to MODIS resolution, and LWP retrieved from the
833 one-minute radiance values, the LWP is 60%-70% of that obtained using a one-minute moving
834 average of the LWP retrieved at the native resolution. Fully-independent Advanced Microwave
835 Scanning Radiometer-2 (AMSR2) satellite measurements of LWP appear closer to the *in-situ*
836 values in Figs. A2a and A3a, but this may be fortuitous, as the time differences are also larger.
837 MODIS N_d values are consistently less than the vertically-averaged *in situ* values, also seen in
838 (Gryspeerdt et al. 2022). We speculate this is because of the strong dependence on the r_e retrieval.

839 **References**

- 840 Abel, S. J., I. A. Boutle, K. Waite, S. Fox, P. R. Brown, and R. C. et al., 2017: The role of precipita-
841 tion in controlling the transition from stratocumulus to cumulus clouds in a northern hemisphere
842 cold-air outbreak. *J. Atmos. Sci.*, **74**, 2293–2314, <https://doi.org/10.1175/jas-d-16-0362.1>.
- 843 Adebisi, A. A., P. Zuidema, I. Chang, S. P. Burton, and B. Cairns, 2020: Mid-level clouds are
844 frequent above the southeast atlantic stratocumulus clouds. *Atmos. Chem. Phys.*, **20**, 11 025–
845 11 043, <https://doi.org/10.5194/acp-20-11025-2020>.
- 846 Alexandrov, M., B. Cairns, A. Wasilewski, A. Ackerman, M. McGill, and e. a. J. Yorks, J., 2015:
847 Liquid water cloud properties during the polarimeter definition experiment (PODEX). *Rem.*
848 *Sens. Env.*, **169**, 20–36.
- 849 Alexandrov, M. D., B. Cairns, C. Emde, A. S. Ackerman, and B. van Diedenhoven, 2012: Accuracy
850 assessments of cloud droplet size retrievals from polarized reflectance measurements by the
851 research scanning polarimeter. *Rem. Sens. Env.*, **125**, 92–111.
- 852 Alexandrov, M. D., and Coauthors, 2018: Retrievals of cloud droplet size from the research
853 scanning polarimeter data: Validation using in situ measurements. *Remote Sens. Environ.*, **210**,
854 76–95, <https://doi.org/10.1016/j.rse.2018.03.005>.
- 855 Atlas, R. L., C. S. Bretherton, M. F. Khairoutdinov, and P. N. Blossey, 2022: Hallett-mossop
856 rime splintering dims cumulus clouds over the southern ocean: New insight from nudged global
857 storm-resolving simulations. *AGU Advances*, **3**, <https://doi.org/10.1029/2021AV000454>.
- 858 Bigg, E. K., 1953: The supercooling of water. *Proc. Phys. Soc.*, **66B**, 688–694, [https://doi.org/](https://doi.org/10.1088/0370-1301/66/8/309)
859 [10.1088/0370-1301/66/8/309](https://doi.org/10.1088/0370-1301/66/8/309).
- 860 Bodas-Salcedo, A., and Coauthors, 2014: Origins of the solar radiation biases over the southern
861 ocean in CFMIP2 models. *J. Clim.*, **27**, 41– 56, <https://doi.org/10.1175/JCLI-D-13-00169.1>.
- 862 Chellini, G., R. R. Gierens, and S. Kneifel, 2022: Ice aggregation in low-level mixed-phase clouds
863 at a high Arctic site: Enhanced by dendritic growth and absent close to the melting level. *J.*
864 *Geophys. Res.*, **127**.

- 865 Chou, S. H., and M. P. Ferguson, 1991: Heat fluxes and roll circulations over the western Gulf
866 Stream during an intense cold-air outbreak. *Bound.-Layer Meteor.*, **55**, 255–281.
- 867 Choularton, T. W., D. J. Griggs, B. Y. Humood, and J. Latham, 1980: Laboratory studies of riming,
868 and its relation to ice splinter production. *Q. J. Roy. Meteor. Soc.*, **106**, 367–374, [https://doi.org/](https://doi.org/10.1002/qj.49710644809)
869 [10.1002/qj.49710644809](https://doi.org/10.1002/qj.49710644809).
- 870 Christensen, M. W., W. K. Jones, and P. Stier, 2020: Aerosols enhance cloud lifetime and brightness
871 along the stratus-to-cumulus transition. *PNAS*, **117**, 17,591–17,598, [https://doi.org/10.1073/](https://doi.org/10.1073/pnas.1921231117)
872 [pnas.1921231117](https://doi.org/10.1073/pnas.1921231117).
- 873 Cooper, W. A., 1986: Ice initiation in natural clouds. *Precipitation Enhancement—A Scientific*
874 *Challenge, Meteor. Monogr.*, 29–32.
- 875 Corral, A. F., and Coauthors, 2021: An overview of atmospheric features over the Western North
876 Atlantic Ocean and North American East Coast – Part 1: Analysis of aerosols, gases, and wet
877 deposition chemistry. *J. Geophys. Res.*, **126**, <https://doi.org/10.1029/2020JD032592>.
- 878 Dadashazar, H., and Coauthors, 2021: Cloud drop number concentrations over the western north
879 atlantic ocean: Seasonal cycle, aerosol interrelationships, and other influential factors. *Atmos.*
880 *Chem. Phys.*, **21**, 10 499–10 526, <https://doi.org/10.5194/acp-21-10499-2021>.
- 881 DeMott, P. J., T. Hill, C. McCluskey, K. Prather, D. Collins, and R. S. et al., 2016: Sea spray
882 aerosol as a unique source of ice nucleating particles. *PNAS*, **113**, 5797–5803.
- 883 Dirks, R., J. P. Kuettner, and J. A. Moore, 1988: Genesis of Atlantic Lows Experiment (GALE):
884 An Overview. *Bull. Amer. Meteorol. Soc.*, **69**, 148–160.
- 885 Duscha, C., C. Barrell, I. A. Renfrew, I. Brooks, H. Sodemann, and J. Reuder, 2022: A ship-based
886 characterization of coherent boundary-layer structures over the lifecycle of a marine cold-air
887 outbreak. *Bound.-Layer Meteor.*, **183**, 355–380.
- 888 Eirund, G. K., U. Lohmann, and A. Possner, 2019: Cloud ice processes enhance spatial scales of
889 organization in arctic stratocumulus. *Geophys. Res. Lett.*, **46**, 14,109–14,117.
- 890 Fabry, F., and I. Zawadzki, 1995: Long-term radar observations of the melting layer of precipitation
891 and their interpretation. *J. Atmos. Sci.*, **52**, 838–851.

892 Ferrare, R., and Coauthors, 2023: Airborne HSRL-2 measurements of elevated aerosol de-
893 polarization associated with nonspherical sea salt. *Front. Rem. Sens.*, **4**, [https://doi.org/](https://doi.org/10.3389/frsen.2023.1143944)
894 [10.3389/frsen.2023.1143944](https://doi.org/10.3389/frsen.2023.1143944).

895 Field, P. R., and A. J. Heymsfield, 2015: Importance of snow to global precipitation. *Geophys.*
896 *Res. Lett.*, **42**, 9512–9520, <https://doi.org/10.1002/2015GL065497>.

897 Field, P. R., and Coauthors, 2017: Exploring the convective grey zone with regional simulations
898 of a cold air outbreak. *Q.J.R. Meteorol. Soc.*, **143**, 2537–2555, <https://doi.org/10.1002/qj.3105>.

899 Fletcher, J. K., S. L. Mason, and C. Jakob, 2016: A climatology of clouds in marine
900 cold air outbreaks in both hemispheres. *J. Climate*, **29**, 6677–6692, [https://doi.org/10.1175/](https://doi.org/10.1175/JCLI-D-15-0783.1)
901 [JCLI-D-15-0783.1](https://doi.org/10.1175/JCLI-D-15-0783.1).

902 Frey, W. R., A. L. Morrison, J. E. Kay, R. Guzman, and H. Chepfer, 2018: The combined influence
903 of observed southern ocean clouds and sea ice on top-of-atmosphere albedo. *J. Geophys. Res.*,
904 **123**, 4461–4475, <https://doi.org/10.1029/2018JD028505>.

905 Geerts, B., and Coauthors, 2022: The COMBLE Campaign: A Study of Marine Boundary
906 Layer Clouds in Arctic Cold-Air Outbreaks. *Bull. Am. Meteor. Soc.*, **103** (5), E1371 – E1389,
907 <https://doi.org/10.1175/BAMS-D-21-0044.1>.

908 Gettelman, A., and Coauthors, 2010: Global simulations of ice nucleation and ice supersaturation
909 with an improved cloud scheme in the Community Atmosphere Model. *J. Geophys. Res.*, **115**.

910 Gryspeerdt, E., and Coauthors, 2019: Constraining the aerosol influence on cloud liquid water
911 path. *Atmos. Chem. Phys.*, **19**, 5331–5347.

912 Gryspeerdt, E., and Coauthors, 2022: The impact of sampling strategy on the cloud droplet number
913 concentration estimated from satellite data. *Atmos. Meas. Tech.*, **15**, 3875–3892, [https://doi.org/](https://doi.org/10.5194/amt-15-3875-2022)
914 [10.5194/amt-15-3875-2022](https://doi.org/10.5194/amt-15-3875-2022).

915 Hallett, J., and S. C. Mossop, 1974: Production of secondary ice particles during the riming
916 process. *Nature*, **249**, 26–28, <https://doi.org/10.1038/249026a0>.

- 917 Hu, Y., and Coauthors, 2009: CALIPSO/CALIOP Cloud Phase Discrimination Algo-
918 rithm. *J. Atmos. and Ocean. Tech.*, **26**, 2293–2309, [https://doi.org/https://doi.org/10.1175/](https://doi.org/10.1175/2009JTECHA1280.1)
919 2009JTECHA1280.1.
- 920 Irish, V. E., and Coauthors, 2019: Ice nucleating particles in the marine boundary layer in the
921 canadian arctic during summer 2014. *Atmos. Chem. Phys.*, **19**, 1027–1039.
- 922 Jones, C. R., C. S. Bretherton, and D. Leon, 2011: Coupled vs. decoupled boundary layers in
923 VOCALS-REx. *Atmos. Chem. Phys.*, 7143–7153, <https://doi.org/10.5194/acp-11-7143-2011>.
- 924 Järvinen, E., and Coauthors, 2022: Evidence for secondary ice production in southern ocean
925 maritime boundary layer clouds. *J. Geophys. Res.*, **127**.
- 926 Karalis, M., G. Sotiropoulou, S. J. Abel, E. Bossioli, P. Georgakaki, G. Methymaki, A. Nenes, and
927 M. Tombrou, 2022: Effects of secondary ice processes on a stratocumulus to cumulus transition
928 during a cold-air outbreak. *Atmos. Res.*, **277**, [https://doi.org/https://doi.org/10.1016/j.atmosres.](https://doi.org/10.1016/j.atmosres.2022.106302)
929 2022.106302.
- 930 Kirschler, S., and Coauthors, 2022: Seasonal updraft speeds change cloud droplet number concen-
931 trations in low-level clouds over the western north atlantic. *Atmos. Chem. Phys.*, **22**, 8299–8319,
932 <https://doi.org/10.5194/acp-22-8299-2022>.
- 933 Kirschler, S., and Coauthors, 2023: Overview and statistical analysis of boundary layer clouds and
934 precipitation over the western north-atlantic ocean. *Atmos. Chem. Phys. Disc.*, [https://doi.org/](https://doi.org/10.5194/egusphere-2023-898)
935 10.5194/egusphere-2023-898.
- 936 Korolev, A., and Coauthors, 2020: A new look at the environmental conditions favorable
937 to secondary ice production. *Atmos. Chem. Phys.*, **20**, 1391–1429, [https://doi.org/10.5194/](https://doi.org/10.5194/acp-20-1391-2020)
938 acp-20-1391-2020.
- 939 Lance, S., 2012: Coincidence errors in a Cloud Droplet Probe (CDP) and a Cloud and Aerosol
940 Spectrometer (CAS), and the Improved Performance of a Modified CDP. *J. Atmos. Oceanic*
941 *Tech.*, **29**, 1532–1541, <https://doi.org/10.1175/JTECH-D-11-00208.1>.
- 942 Lauber, A., A. Kiselev, T. Pander, P. Handmann, and T. Leisner, 2018: Secondary ice formation
943 during freezing of levitated droplets. *J. Atmos. Sci.*, **75**, 2815–2826.

- 944 Lawson, P., and P. Zuidema, 2009: Aircraft microphysical and surface-based radar observations of
945 summertime arctic clouds. *J. Atmos. Sci.*, **66**, 3505–3529, <https://doi.org/10.1175/2009JAS3177>.
946 1.
- 947 Liu, J., S. Xie, J. R. Norris, and S. Zhang, 2014: Low-level cloud response to the gulf stream front
948 in winter using CALIPSO. *J. Clim.*, **27**, 4421–4432.
- 949 Luke, E. P., F. Yang, P. Kollias, A. Vogelmann, and M. Maahn, 2021: New insights into ice
950 multiplication using remote-sensing observations of slightly supercooled mixedphase clouds in
951 the arctic. *Proc. Natl. Acad. Sci.*, **118**, <https://doi.org/10.1073/pnas.2021387118>.
- 952 Mages, Z., P. Kollias, Z. Zhu, and E. P. Luke, 2023: Surface-based observations of cold-air
953 outbreak clouds during the COMBLE field campaign. *Atmos. Chem. Phys.*, **23**, 3561–3574,
954 <https://doi.org/10.5194/acp-23-3561-2023>.
- 955 Matus, A. V., and T. S. L'Ecuyer, 2017: The role of cloud phase in earth's radiation budget. *J.*
956 *Geophys. Res.*, **122**, 2559–2578, <https://doi.org/10.1002/2016JD025951>.
- 957 McCluskey, C. S., T. C. Hill, R. Humphries, A. Rauker, S. Moreau, and P. S. et al., 2018:
958 Observations of ice nucleating particles over southern ocean waters. *Geophys. Res. Lett.*, **45**,
959 11 989–11 997, <https://doi.org/10.1029/2018GL079981>.
- 960 McFarquhar, G. M., C. S. Bretherton, R. Marchand, A. Protat, P. DeMott, and S. A. et al., 2021:
961 Observations of clouds, aerosols, precipitation, and surface radiation over the southern ocean:
962 An overview of CAPRICORN, MARCUS, MICRE and SOCRATES. *Bull. Am. Meteor. Soc.*,
963 **102**, E894–E928, <https://doi.org/10.1175/bams-d-20-0132.1>.
- 964 McGraw, Z., T. Strovelmo, L. Polvani, S. Hofer, J. Shaw, and A. Gettelman, 2023: On the links
965 between ice nucleation, cloud phase and climate sensitivity in CESM2. *Geophys. Res. Lett.*, **123**.
- 966 Meyers, M. P., R. L. Walko, J. Y. Harrington, and W. R. Cotton, 1997: New RAMS cloud
967 microphysics parameterization. Part II: The two-moment scheme. *Atmos. Res.*, **45**, 3–39.
- 968 Milbrandt, J. A., and H. Morrison, 2016: Parameterization of cloud microphysics based on the
969 prediction of bulk ice particle properties. part iii: Introduction of multiple free categories. *J.*
970 *Atmos. Sci.*, **73**, 975–995.

971 Minobe, S., A. Kuwano-Yoshida, and N. K. et al., 2008: Influence of the gulf stream on the
972 troposphere. *Nature*, **452**, 206–209, <https://doi.org/10.1038/nature06690>.

973 Mitchell, J. F. B., C. A. Senior, and W. J. Ingram, 1989: CO₂ and climate: A missing feedback?
974 *Nature*, **341**, <https://doi.org/10.1038/341132a0>.

975 Mossop, S. C., 1976: Production of secondary ice particles during the growth of graupel by riming.
976 *Quart. J. Met. Soc.*, **102**, 45–47.

977 Mülmstadt, J., O. Sourdeval, J. Delano, and J. Quaas, 2015: Frequency of occurrence of rain
978 from liquid-, mixed-, and ice-phase clouds derived from A-Train satellite retrievals. *Geophys.*
979 *Res. Lett.*, **42**, 6502–6509, <https://doi.org/10.1002/2015GL064604>.

980 Murray-Watson, R. J., E. Gryspeerdt, and T. Goren, 2023: Investigating the development of clouds
981 within marine cold air outbreaks. *Atmos. Chem. Phys. Disc.*

982 Naud, C. M., J. F. Booth, K. Lamer, R. Marchand, A. Protat, and G. McFarquhar, 2020: On the
983 relationship between the marine cold air outbreak m parameter and low-level cloud heights in
984 the midlatitudes. *J. Geophys. Res.*, **125**, <https://doi.org/10.1029/2020JD032465>.

985 Painemal, D., and P. Zuidema, 2011: Assessment of MODIS cloud effective radius and optical
986 thickness retrievals over the Southeast Pacific with VOCALS-REx in-situ measurements. *J.*
987 *Geophys. Res.*, **116**, <https://doi.org/10.1029/2011JD016155>.

988 Painemal, D., and Coauthors, 2021: Evaluation of satellite retrievals of liquid clouds from the
989 GOES-13 imager and MODIS over the midlatitude North Atlantic during the NAAMES cam-
990 paign. *Atmos. Meas. Tech.*, **14**, 6633–6646.

991 Painemal, D., and Coauthors, 2023: Wintertime synoptic patterns of variability of midlatitude
992 boundary layer clouds over the western North Atlantic: Climatology and insights from in-situ
993 ACTIVATE observations. *J. Geophys. Res.*, <https://doi.org/10.1029/2022JD037725>.

994 Papritz, L., S. Pfahl, H. Sodemann, and H. Wernli, 2015: A climatology of cold air outbreaks and
995 their impact on air–sea heat fluxes in the high-latitude south pacific. *J. Climate*, **28**, 342–364,
996 <https://doi.org/10.1175/JCLI-D-14-00482.1>.

- 997 Plagge, A., J. B. Edson, and D. Vandemark, 2016: In situ and satellite evaluation of air–sea
998 flux variation near ocean temperature gradients. *J. Climate*, **29**, 1583–1602, [https://doi.org/](https://doi.org/10.1175/jcli-d-15-0489.1)
999 10.1175/jcli-d-15-0489.1.
- 1000 Seethala, C., and Coauthors, 2021: On assessing ERA5 and MERRA2 representations of
1001 cold-air outbreaks across the Gulf Stream. *Geophys. Res. Lett.*, **48**, [https://doi.org/10.1029/](https://doi.org/10.1029/2021GL094364)
1002 2021GL094364.
- 1003 Small, R. J., S. P. deSzoek, S. P. Xie, L. O’Neill, H. Seo, and Q. e. a. Q. Song, 2008: Air-sea
1004 interaction over ocean fronts and eddies. *Dynamics of Atmospheres and Oceans*, **45**, 274–319,
1005 <https://doi.org/10.1016/j.dynatmoce.2008.01.001>.
- 1006 Sorooshian, A., and Coauthors, 2019: Aerosol-Cloud-Meteorology Interaction Airborne Field
1007 Investigations: Using lessons learned from the US west coast in the design of ACTIVATE off the
1008 east coast. *Bull. Am. Meteor. Soc.*, **100**, 1512–1528, [https://doi.org/10.1175/BAMS-D-18-0100.](https://doi.org/10.1175/BAMS-D-18-0100.1)
1009 1.
- 1010 Sorooshian, A., and Coauthors, 2023: Spatially-coordinated airborne data and complementary
1011 products for aerosol, gas, cloud, and meteorological studies: The NASA ACTIVATE dataset.
1012 *Earth Sys. Sci. Data*, <https://doi.org/10.5194/essd-2023-109>.
- 1013 Sotiropoulou, G., S. Sullivan, J. Savre, G. Lloyd, T. Lachlan-Cope, A. Ekman, and A. Nenes,
1014 2020: The impact of secondary ice production on Arctic stratocumulus. *Atmos. Chem. Phys.*,
1015 **20**, 1301–1316, <https://doi.org/10.5194/acp-20-1301-2020>.
- 1016 Takahashi, T., Y. Nagao, and Y. Kushiyama, 1995: Possible high ice particle production during
1017 graupel–graupel collisions. *J. Atmos. Sci.*, **52**, 4523–4527, [https://doi.org/10.1175/1520-0469.](https://doi.org/10.1175/1520-0469.1995.015200469.1)
- 1018 Tan, I., T. Storelvmo, and M. D. Zelinka, 2016: Observational constraints on mixed-phase clouds
1019 imply higher climate sensitivity. *Science*, **352**, 224–227.
- 1020 Terai, C. R., Y. Zhang, S. A. Klein, M. D. Zelinka, J. C. Chiu, and Q. Min, 2019: Mechanisms
1021 behind the extratropical stratiform low-cloud optical depth response to temperature in ARM site
1022 observations. *J. Geophys. Res.*, **124**, 2127–2147.

- 1023 Thornhill, K. L., B. E. Anderson, J. Barrick, D. Bagwell, R. Friesen, and D. Lenschow, 2003:
1024 Air motion intercomparison flights during Transport and Chemical Evolution in the Pacific
1025 (TRACE-P)/ACE-ASIA. *J. Geophys. Res.*, **108**, <https://doi.org/10.1029/2002JD003108>.
- 1026 Tornow, F., A. S. Ackerman, and A. M. Fridlind, 2021: Preconditioning of overcast-to-broken cloud
1027 transitions by riming in marine cold air outbreaks. *Atmos. Chem. Phys.*, **21**, 12 049–12 067.
- 1028 Tornow, F., and Coauthors, 2022: Dilution of boundary layer cloud condensation nucleus concen-
1029 trations by free tropospheric entrainment during marine cold air outbreaks. *Geophys. Res. Lett.*,
1030 **49**, <https://doi.org/10.1029/2022GL098444>.
- 1031 Vaillant de Guélis, T., A. Schwarzenböck, V. Shcherbakov, C. Gourbeyre, B. Laurent, R. Dupuy,
1032 P. Coutris, and C. Duroure, 2019: Study of the diffraction pattern of cloud particles and the
1033 respective responses of optical array probes. *Atmos. Meas. Tech.*, **12**, 2513–2529, [https://doi.org/](https://doi.org/10.5194/amt-12-2513-2019)
1034 [10.5194/amt-12-2513-2019](https://doi.org/10.5194/amt-12-2513-2019).
- 1035 Vömel, H., A. Sorooshian, C. Robinson, T. J. Shingler, K. L. Thornhill, and L. D. Ziemba, 2023:
1036 Dropsonde observations during the Aerosol Cloud meTeorology Interactions oVer the western
1037 Atlantic Experiment. *Scientific Data*, <https://doi.org/10.1038/s41597-023-02647-5>.
- 1038 Wall, C. J., T. Storelvmo, J. R. Norris, and I. Tan, 2022: Observational constraints on southern
1039 ocean cloud-phase feedback. *J. Clim.*, **35**, 5087–5102.
- 1040 Welti, A., and Coauthors, 2020: Ship-based measurements of ice nuclei concentrations over the
1041 arctic, atlantic, pacific and southern oceans. *Atmos. Chem. Phys.*, **20**, 15 191–15 206.
- 1042 Wendisch, M., and Coauthors, 2019: The arctic cloud puzzle: Using acloud/pascal multiplatform
1043 observations to unravel the role of clouds and aerosol particles in arctic amplification. *Bull. Am.*
1044 *Meteor. Soc.*, **100 (5)**, 841 – 871, <https://doi.org/10.1175/BAMS-D-18-0072.1>.
- 1045 Wood, R., C. S. Bretherton, D. Leon, A. D. Clarke, P. Zuidema, G. Allen, and H. Coe,
1046 2011: An aircraft case study of the spatial transition from closed to open mesoscale cellu-
1047 lar convection over the Southeast Pacific. *Atmos. Chem. Phys.*, **11**, 2341–2370, [https://doi.org/](https://doi.org/10.5194/acp-11-2341-2011)
1048 [10.5194/acp-11-2341-2011](https://doi.org/10.5194/acp-11-2341-2011).
- 1049 Yang, C., M. Diao, A. Gettelman, K. Zhang, J. Sun, G. McFarquhar, and W. Wu, 2021: Ice and
1050 supercooled liquid water distributions over the southern ocean based on in situ observations and

1051 climate model simulations. *J. Geophys. Res.*, **126**, e2021JD036045, [https://doi.org/10.1029/](https://doi.org/10.1029/2021JD036045)
1052 2021JD036045.

1053 Young, G., and Coauthors, 2016: Observed microphysical changes in arctic mixed-phase clouds
1054 when transitioning from sea ice to open ocean. *Atmos. Chem. Phys.*, **16**, 13,945–13,967,
1055 <https://doi.org/10.5194/acp-16-13945-2016>.

1056 Young, G. S., D. A. R. Kristovich, M. R. Hjelmfelt, and R. C. Foster, 2002: Rolls, streets, waves,
1057 and more: A review of quasi-two-dimensional structures in the atmospheric boundary layer.
1058 *Bull. Am. Meteor. Soc.*, **83**, 997 – 1002, [https://doi.org/https://doi.org/10.1175/1520-0477\(2002\)](https://doi.org/10.1175/1520-0477(2002)083<0997:RSWAMA>2.3.CO;2)
1059 083<0997:RSWAMA>2.3.CO;2.

1060 Zaremba, T. J., R. M. Rauber, G. M. McFarquhar, P. J. DeMott, J. J. D'Alessandro, and W. Wu,
1061 2021: Ice in southern ocean clouds with cloud top temperatures exceeding - 5 Celsius. *J.*
1062 *Geophys. Res.*, **126**, <https://doi.org/10.1029/2021JD034574>.

1063 Zelinka, M., T. A. Myers, D. T. McCoy, S. Po-Chedley, P. M. Caldwell, and P. C. et al., 2020:
1064 Causes of higher climate sensitivity in CMIP6 models. *Geophys. Res. Lett.*, **47**, [https://doi.org/](https://doi.org/10.1029/2019GL085782)
1065 10.1029/2019GL085782.

1066 Zhao, X., and X. Liu, 2022: Primary and secondary ice production: interactions and their relative
1067 importance. *Atmos. Chem. Phys.*, **22**, 2585–2600, <https://doi.org/10.5194/acp-22-2585-2022>.

1068 Zuidema, P., and K. F. Evans, 1998: On the validity of the independent pixel approximation for
1069 boundary layer clouds observed during ASTEX. *J. Geophys. Res.*, **103**, 6059–6074.

1070 Zuidema, P., D. Painemal, S. deSzoek, and C. Fairall, 2009: Stratocumulus cloud top height
1071 estimates and their climatic implications. *J. Clim.*, **22**, 4652–4666, [https://doi.org/10.1175/](https://doi.org/10.1175/2009JCLI2708.1)
1072 2009JCLI2708.1.